



Adiabatic-connection fluctuation-dissipation DFT for the structural properties of solids - The renormalized ALDA and electron gas kernels

Patrick, Christopher E.; Thygesen, Kristian Sommer

Published in:
Journal of Chemical Physics

Link to article, DOI:
[10.1063/1.4919236](https://doi.org/10.1063/1.4919236)

Publication date:
2015

Document Version
Publisher's PDF, also known as Version of record

[Link back to DTU Orbit](#)

Citation (APA):
Patrick, C. E., & Thygesen, K. S. (2015). Adiabatic-connection fluctuation-dissipation DFT for the structural properties of solids - The renormalized ALDA and electron gas kernels. *Journal of Chemical Physics*, 143(10), Article 102802. <https://doi.org/10.1063/1.4919236>

General rights

Copyright and moral rights for the publications made accessible in the public portal are retained by the authors and/or other copyright owners and it is a condition of accessing publications that users recognise and abide by the legal requirements associated with these rights.

- Users may download and print one copy of any publication from the public portal for the purpose of private study or research.
- You may not further distribute the material or use it for any profit-making activity or commercial gain
- You may freely distribute the URL identifying the publication in the public portal

If you believe that this document breaches copyright please contact us providing details, and we will remove access to the work immediately and investigate your claim.

Adiabatic-connection fluctuation-dissipation DFT for the structural properties of solids—The renormalized ALDA and electron gas kernels

Christopher E. Patrick and Kristian S. Thygesen

Citation: *The Journal of Chemical Physics* **143**, 102802 (2015); doi: 10.1063/1.4919236

View online: <http://dx.doi.org/10.1063/1.4919236>

View Table of Contents: <http://scitation.aip.org/content/aip/journal/jcp/143/10?ver=pdfcov>

Published by the AIP Publishing

Articles you may be interested in

Stability conditions for exact-exchange Kohn-Sham methods and their relation to correlation energies from the adiabatic-connection fluctuation-dissipation theorem

J. Chem. Phys. **141**, 204107 (2014); 10.1063/1.4901924

Evidence of scaling in the high pressure phonon dispersion relations of some elemental solids

J. Chem. Phys. **141**, 044714 (2014); 10.1063/1.4890998

Structural, electronic and elastic properties of Fe-doped YN: DFT study

AIP Conf. Proc. **1536**, 1085 (2013); 10.1063/1.4810612

A DFT study on structural, vibrational properties, and quasiparticle band structure of solid nitromethane

J. Chem. Phys. **138**, 184705 (2013); 10.1063/1.4803479

Structural and vibrational properties of solid nitromethane under high pressure by density functional theory

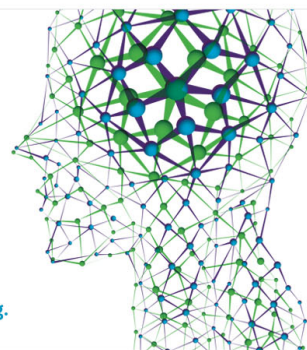
J. Chem. Phys. **124**, 124501 (2006); 10.1063/1.2179801

How can you **REACH 100%**
of researchers at the Top 100
Physical Sciences Universities? (TIMES HIGHER EDUCATION RANKINGS, 2014)

With *The Journal of Chemical Physics*.

AIP | The Journal of
Chemical Physics

THERE'S POWER IN NUMBERS. Reach the world with AIP Publishing.



Adiabatic-connection fluctuation-dissipation DFT for the structural properties of solids—The renormalized ALDA and electron gas kernels

Christopher E. Patrick^{a)} and Kristian S. Thygesen^{b)}

Center for Atomic-Scale Materials Design (CAMD), Department of Physics, Technical University of Denmark, DK—2800 Kongens Lyngby, Denmark

(Received 14 November 2014; accepted 16 December 2014; published online 29 April 2015)

We present calculations of the correlation energies of crystalline solids and isolated systems within the adiabatic-connection fluctuation-dissipation formulation of density-functional theory. We perform a quantitative comparison of a set of model exchange-correlation kernels originally derived for the homogeneous electron gas (HEG), including the recently introduced renormalized adiabatic local-density approximation (rALDA) and also kernels which (a) satisfy known exact limits of the HEG, (b) carry a frequency dependence, or (c) display a $1/k^2$ divergence for small wavevectors. After generalizing the kernels to inhomogeneous systems through a reciprocal-space averaging procedure, we calculate the lattice constants and bulk moduli of a test set of 10 solids consisting of tetrahedrally bonded semiconductors (C, Si, SiC), ionic compounds (MgO, LiCl, LiF), and metals (Al, Na, Cu, Pd). We also consider the atomization energy of the H_2 molecule. We compare the results calculated with different kernels to those obtained from the random-phase approximation (RPA) and to experimental measurements. We demonstrate that the model kernels correct the RPA's tendency to overestimate the magnitude of the correlation energy whilst maintaining a high-accuracy description of structural properties. © 2015 AIP Publishing LLC. [<http://dx.doi.org/10.1063/1.4919236>]

I. INTRODUCTION

The remarkable rise of density-functional theory¹ (DFT) in the last few decades owes much to the efficient treatment of exchange and correlation within the local-density approximation (LDA).² However, known deficiencies in the LDA's description of certain systems have led to the development of a hierarchy of exchange-correlation (XC) functionals of varying computational expense.³ At the high-complexity end of this spectrum of functionals lies the adiabatic connection-fluctuation dissipation formulation of DFT (ACFD-DFT),^{4,5} which in its simplest form corresponds to the random-phase approximation (RPA) correlation energy.⁶ “Beyond-RPA” methods strive for an even higher level of accuracy and form an important and fast-developing field of research.^{6–12}

ACFD-DFT provides a natural path for the improvement of the RPA via the introduction of an XC kernel f_{xc} , an ubiquitous quantity in time-dependent DFT (TD-DFT).^{13,14} The homogeneous electron gas (HEG) has become a key system for the development and testing of new kernels through the ACFD-DFT calculation of correlation energies.^{15–18} Jellium slabs also form important test systems, through the ACFD-DFT calculation of their surface energies,^{19,20} inter-slab interaction energies,^{21–23} and as benchmarks for widely used semilocal XC functionals.^{24,25} However, the last few years have seen the application of the ACFD-DFT formalism to calculate the correlation energies of atoms, molecules, and solids, with promising results.^{26–29}

One such example is the “renormalized kernel approach,” which was introduced based on a model XC-kernel named the renormalized adiabatic LDA (rALDA).^{30,31} The rALDA exploits the accurate reciprocal-space description of HEG correlation provided by the adiabatic LDA (ALDA) in the long-wavelength limit, whilst correcting the ALDA's unphysical behavior at short wavelengths. The rALDA and its generalized-gradient analogue (rAPBE) have been shown to yield highly accurate atomization and cohesive energies of molecules and solids.^{30–32}

It is interesting to place the rALDA into the context of other HEG kernels. Many theoretical studies have explored the properties of the exact XC-kernel and derived certain limits which are not necessarily obeyed by the rALDA.^{33–35} Similarly, the rALDA is static, and apart from studies of the HEG,¹⁵ there is little known about dynamical effects on ACFD-DFT correlation energies. Furthermore, the XC-kernel of an insulator is known to behave qualitatively differently to a metallic system like the HEG,³⁶ with the XC-kernel of an insulator famously diverging $\propto 1/k^2$ in the limit of small wavevectors k .³⁷ In this respect, it is important to test the validity of applying a model HEG kernel to non-metallic systems.

This work explores the above aspects through a quantitative comparison of model HEG XC-kernels. Within our sample of XC-kernels, we include the rALDA,³⁰ and also a kernel which satisfies exact limits of the HEG,¹⁷ a simple dynamical kernel,¹⁶ and a kernel which has a divergence $\propto 1/k^2$ when describing an insulator.³⁸ For each XC-kernel, we use ACFD-DFT to calculate the correlation energy of a test set of 10 crystalline solids and evaluate the lattice constant and bulk modulus, which we then compare to calculations using

^{a)}chripa@fysik.dtu.dk

^{b)}thygesen@fysik.dtu.dk

semilocal functionals and the RPA, and also to experiment. We also provide a demonstrative calculation of the atomization energy of the hydrogen molecule to highlight the importance of spin-polarization. We find that all of the model XC-kernels greatly improve the magnitude of the RPA correlation energy whilst providing a highly accurate description of structural properties.

Our study is organized as follows. In Sec. II, we review ACFD-DFT and the role played by the XC-kernel. In particular, we describe the expected behavior of the XC-kernel for the HEG at certain limits (Sec. II C), introduce our chosen set of model kernels (Sec. II D), and apply them to the HEG (Sec. II E). For inhomogeneous systems, we require a scheme to generalize HEG kernels for a varying density; in Sec. II G, we discuss possible schemes and justify the choice made in this work. Section III contains the results of our study, in which we discuss the calculated lattice constants and bulk moduli, absolute correlation energies, and the H₂ molecule. Finally in Sec. IV, we summarize our results and offer our conclusions.

II. THEORY

A. Correlation energies in the ACFD-DFT framework

Here, we summarize the essential concepts of ACFD-DFT. Full derivations may be found in original articles^{4,5} or recent reviews, e.g., Refs. 6 and 39.

In ACFD-DFT, a system of fully interacting electrons is described by a coupling-constant dependent Hamiltonian $H(\lambda)$. The coupling constant λ takes values between 0 and 1 and defines an effective interaction between electrons as λv_c , where v_c is the Coulomb interaction. $H(\lambda = 1)$ corresponds to the exact Hamiltonian of the fully interacting system. In addition to the effective Coulomb interaction, $H(\lambda)$ contains a λ -dependent single-particle potential v_{ext}^λ , constructed in such a way that the ground-state solution of $H(\lambda)$ has exactly the same electronic density as the ground-state solution of the fully interacting ($\lambda = 1$) Hamiltonian. The fixed-density path connecting $\lambda = 0$ and 1 defines the “adiabatic connection.” Since $H(\lambda = 0)$ describes a system of non-interacting electrons with a fully interacting density, $v_{\text{ext}}^{\lambda=0}$ is readily identified as the Kohn-Sham potential from DFT.^{1,2}

Invoking the Hellmann-Feynman theorem, integrating with respect to λ along the adiabatic connection, and comparing to standard DFT¹ yields an expression for the XC energy in terms of the operator describing density fluctuations. The fluctuation-dissipation theorem⁴⁰ provides the link between this operator and the frequency integral of a response function χ^λ . For non-interacting electrons, $\chi^{\lambda=0} \equiv \chi_{\text{KS}}$, the Kohn-Sham response function of time-dependent DFT.^{13,14} The XC-energy is then written as the sum of an “exact” exchange contribution E_x and the correlation energy E_c , where the latter is given by (in Hartree units)

$$E_c = -\frac{1}{2\pi} \sum_{\mathbf{q}} \int_0^1 d\lambda \int_0^\infty ds \times \text{Tr} [v_c(\mathbf{q})(\chi^\lambda(\mathbf{q}, is) - \chi_{\text{KS}}(\mathbf{q}, is))]. \quad (1)$$

Equation (1) has been written in a plane-wave basis so that the quantities on the right-hand side are matrices in the reciprocal

lattice vectors \mathbf{G} and \mathbf{G}' , and the wavevectors \mathbf{q} belong to the first Brillouin zone. The Coulomb interaction is diagonal in a plane-wave representation with elements $4\pi/|\mathbf{q} + \mathbf{G}|^2$, and s is a real number corresponding to an imaginary frequency, $\omega = is$.

The link between the interacting and non-interacting response functions is supplied by linear-response theory,¹⁴ which describes the behavior of density n in the presence of a small perturbation,

$$\delta n(\mathbf{q}, \omega) = \chi^\lambda(\mathbf{q}, \omega) \delta v_{\text{ext}}^\lambda(\mathbf{q}, \omega). \quad (2)$$

The fact that χ^λ yields the exact density response at all values of λ allows the link to be made to χ_{KS} through the following integral equation:

$$\chi^\lambda(\mathbf{q}, \omega) = \chi_{\text{KS}}(\mathbf{q}, \omega) + \chi_{\text{KS}}(\mathbf{q}, \omega) f_{\text{Hxc}}^\lambda(\mathbf{q}, \omega) \chi^\lambda(\mathbf{q}, \omega), \quad (3)$$

where the Hartree-XC kernel f_{Hxc}^λ has been introduced as

$$f_{\text{Hxc}}^\lambda(\mathbf{q}, \omega) = \lambda v_c(\mathbf{q}) + f_{xc}^\lambda(\mathbf{q}, \omega). \quad (4)$$

The XC-kernel f_{xc}^λ describes the change in the XC-potential v_{xc}^λ upon perturbing the density, which is a fully nonlocal quantity in time and space,¹⁴

$$f_{xc}^\lambda(\mathbf{r}, \mathbf{r}', t - t') = \frac{\delta v_{xc}^\lambda(\mathbf{r}, t)}{\delta n(\mathbf{r}', t')}. \quad (5)$$

By assuming approximate forms for χ_{KS} and f_{xc}^λ , one can use Eq. (3) to calculate χ^λ and thus evaluate the correlation energy with Eq. (1).

B. ACFD-DFT in practice

In a plane-wave basis, the Kohn-Sham response function has the form⁴¹

$$\chi_{\text{KS}}^{\text{GG}'}(\mathbf{q}, is) = \frac{2}{\Omega} \sum_{\mathbf{k}, \nu, \nu'} (f_{\nu\mathbf{k}} - f_{\nu'\mathbf{k}+\mathbf{q}}) \times \frac{n_{\nu\mathbf{k}, \nu'\mathbf{k}+\mathbf{q}}(\mathbf{G}) n_{\nu\mathbf{k}, \nu'\mathbf{k}+\mathbf{q}}^*(\mathbf{G}')}{is + \varepsilon_{\nu\mathbf{k}} - \varepsilon_{\nu'\mathbf{k}+\mathbf{q}}}, \quad (6)$$

where $f_{\nu\mathbf{k}}$ and $\varepsilon_{\nu\mathbf{k}}$ represent the occupation factor and energy of the Kohn-Sham state $\psi_{\nu\mathbf{k}}$, while the pair densities $n_{\nu\mathbf{k}, \nu'\mathbf{k}+\mathbf{q}}(\mathbf{G})$ are matrix elements of plane waves, $\langle \psi_{\nu\mathbf{k}} | e^{-i(\mathbf{q}+\mathbf{G})\cdot\mathbf{r}} | \psi_{\nu'\mathbf{k}+\mathbf{q}} \rangle$. Ω is the volume of the primitive unit cell, and the factor of 2 assumes a spin-degenerate system. From Eqs. (1) and (6), the benefits of the ACFD-DFT are not very obvious; to construct χ_{KS} , we require ψ , which means solving the Kohn-Sham equations and thus already obtaining the correlation energy. Furthermore, to solve the integral equation (3), we require the XC-kernel f_{xc} , which arguably is even more complicated than the XC-potential v_{xc} due to its frequency dependence.

However, the attraction of ACFD-DFT is that even setting $f_{xc} = 0$ yields both a nonlocal description of exchange and a nontrivial expression for the correlation energy, namely, that obtained from the RPA,⁶

$$E_c^{\text{RPA}} = \frac{1}{2\pi} \sum_{\mathbf{q}} \int_0^\infty ds \text{Tr} [\ln \{1 - v_c(\mathbf{q}) \chi_{\text{KS}}(\mathbf{q}, is)\} + v_c(\mathbf{q}) \chi_{\text{KS}}(\mathbf{q}, is)]. \quad (7)$$

The RPA has been applied across a wide range of physical systems^{42–49} and found to give a markedly improved description of nonlocal correlation effects. Equation (7) is usually applied as a post-processing step to a DFT calculation, analogous to G_0W_0 corrections to band gaps.^{50,51}

Based on the success of the RPA, it may be hoped that the description of correlation might be further improved by using more sophisticated approximations for f_{xc} . While it turns out that the ALDA offers little improvement,²⁷ nonlocal, dynamical, and/or energy-optimized approximations for f_{xc} have been found to correct deficiencies of the RPA when calculating the correlation energy of the HEG.^{15–23}

We note that a non-self-consistent application of the ACFD-DFT formula might suffer from a dependence on v_{xc} , the exchange-correlation potential used to construct the orbitals forming χ_{KS} . In this respect, a self-consistent scheme is attractive and the subject of current research.^{52–55} However, here, we do not include any self-consistency and treat f_{xc} as a quantity to be optimized independent of the v_{xc} used to generate χ_{KS} .⁵⁶

C. XC-kernels from the homogeneous electron gas

In the same way that the HEG is used to generate approximate XC-potentials, it also forms a natural starting point for approximate XC-kernels. Here, we review some properties of the exact XC-kernel of the HEG.

1. Definitions

The analogue of Eq. (3) for the HEG is

$$\chi^\lambda(k, \omega) = \chi_0(k, \omega) + \chi_0(k, \omega) f_{Hxc}^{\text{HEG}, \lambda}(k, \omega) \chi^\lambda(k, \omega). \quad (8)$$

All quantities appearing in this equation are scalars, with $k = |\mathbf{G} + \mathbf{q}|$. χ_0 is the Lindhard response function, with occupation numbers equal to 1 for plane-wave states below the Fermi level and zero otherwise.⁵⁷ As demonstrated in the appendix of Ref. 58, in the case that Eq. (3) is applied to the HEG, the Lindhard and Kohn-Sham response functions coincide, so that the quantity $f_{Hxc}^{\text{HEG}, \lambda}$ appearing in Eq. (8) must also match its counterpart f_{Hxc}^h in Eq. (3). Therefore, the HEG forms a rigorous test ground for model XC kernels.

For simplicity, we denote $f_{xc}^{\text{HEG}, \lambda=1}$ as f_{xc}^{HEG} . The local field factor $G(k, \omega)$ is related to $f_{xc}^{\text{HEG}}(k, \omega)$ as $f_{xc}^{\text{HEG}}(k, \omega) = -v_c(k) G(k, \omega)$, so that Eq. (8) defines G in terms of the response functions $\chi^{\lambda=1}$ and χ_0 .³⁴ A potential source of confusion is that another field factor G_I can be found in the literature which has a different defining equation.^{18,34,59,60} For G_I , the Lindhard response function appearing in Eq. (8) is modified such that the occupation numbers of each plane-wave state are calculated using the many-body wavefunction of the fully interacting system.⁵⁹ Therefore, $f_{xc}^{\text{HEG}, I}$ is also a distinct quantity. However, the kernels investigated in this work were derived based on the equivalence of Eqs. (3) and (8) for the HEG,⁵⁸ so it is G which is of interest in the current work.

2. Exact limits

The local-field factor G (and thus f_{xc}^{HEG}) have been the subject of many theoretical studies (cf. Sec. III C of Ref. 33),

and their behavior at certain limits is known exactly. First, in the long wavelength ($k \rightarrow 0$) and static ($\omega = 0$) limit, the HEG XC-kernel reduces to the ALDA,

$$f_{xc}^{\text{HEG}}(k \rightarrow 0, \omega = 0) = f_{xc}^{\text{ALDA}} \equiv -\frac{4\pi A}{k_F^2}, \quad (9)$$

where

$$A = \frac{1}{4} - \frac{k_F^2}{4\pi} \frac{d^2(n\varepsilon_c)}{dn^2}. \quad (10)$$

$k_F = (3\pi^2 n)^{1/3}$ is the Fermi wavevector for the HEG of density n , and ε_c is the correlation energy per electron. The two terms in Eq. (10) correspond to the exchange and correlation contributions to the ALDA kernel. Equation (9) can be seen either as a consequence of the compressibility sum rule³³ or more simply by noting that the ALDA should be exact in describing the HEG response to a uniform, static field.¹⁶

Remaining in the static case but considering small wavelengths ($k \rightarrow \infty$) yields^{34,61}

$$f_{xc}^{\text{HEG}}(k \rightarrow \infty, \omega = 0) = -\frac{4\pi B}{k^2} - \frac{4\pi C}{k_F^2}, \quad (11)$$

whilst in the long wavelength, high frequency limit ($k = 0$, $\omega \rightarrow \infty$) f_{xc}^{HEG} is given by³⁵

$$f_{xc}^{\text{HEG}}(k = 0, \omega \rightarrow \infty) = -\frac{4\pi D}{k_F^2}. \quad (12)$$

Although we have not written it explicitly, A , B , C , and D depend on the density of the HEG, or equivalently on the Fermi wavevector or Wigner radius $r_s = (3/4\pi n)^{1/3}$. Practically A , C , and D can be obtained from a parameterization of the HEG correlation energy ε_c , while B additionally requires the momentum distribution and on-top pair-distribution function of the HEG.⁶² In this work, we use the parameterization of ε_c and B from Refs. 63 and 64, respectively.

3. Intermediate k values

In addition to these limits, calculating the correlation energy from Eq. (1) requires an expression for f_{xc}^{HEG} across all k and ω . Reference 64 provided important insight into the HEG XC-kernel with diffusion Monte Carlo calculations of $f_{xc}^{\text{HEG}}(k, \omega = 0)$ for a range of k vectors and densities. Interestingly, one of the conclusions of the work was that in this static limit and for $k \lesssim 2k_F$, f_{xc}^{HEG} could be well-approximated by taking its $k = 0$ limiting form (i.e., the ALDA, Eq. (9)).

4. The large- k limit and the pair-distribution function

According to Eq. (11), the $k \rightarrow \infty, \omega = 0$ limit of f_{xc}^{HEG} is a constant, and thus $G(k, \omega = 0)$ diverges as k^2 . This property appears to have alarming consequences for the pair-distribution function: in Ref. 65, it is shown that a $G(k)$ which diverges for large k will yield a singular pair-distribution function at the origin (see also Refs. 27 and 66). The crucial point to note however is that the relationship in Ref. 65 assumes a frequency-independent $G(k)$, which is not the same as the frequency-dependent $G(k, \omega)$ evaluated at $\omega = 0$, which Eq. (11) describes. This point is discussed further in Ref. 58.

Nonetheless, a frequency-independent model kernel satisfying the exact HEG limits for small and large k at $\omega = 0$ (e.g., the Corradini, del Sole, Onida, and Palumbo (CDOP) kernel¹⁷) will have a badly behaved pair-distribution function, as demonstrated below and in Fig. 2 of Ref. 29. In this respect, and given that the correlation energy is calculated as an integral over frequency, a frequency-averaged $G(k)$ may be a better starting point for model kernels than $G(k, \omega = 0)$. Below, we compare kernels which do or do not satisfy Eq. (11).

D. Model XC kernels

Having introduced the relevant quantities for the HEG, we now describe the XC-kernels investigated in the current work. The XC-kernels are plotted in reciprocal or real space in Figs. 1(a) and 1(b). The reciprocal and real space XC-kernels are related by the Fourier transform

$$f_{xc}(n, k, \omega) = \int d\mathbf{R} e^{-i\mathbf{k} \cdot \mathbf{R}} f_{xc}(n, R, \omega), \quad (13)$$

with $R = |\mathbf{r} - \mathbf{r}'|$.

1. The rALDA kernel

The rALDA³⁰ XC-kernel is given by

$$f_{xc}^{\text{rALDA}}(n, k) = - \left[\theta(k_c - k) \frac{4\pi}{k_c^2} + \theta(k - k_c) \frac{4\pi}{k^2} \right], \quad (14)$$

where the Heaviside function $\theta(x) = 1$ for $x > 0$ and zero otherwise. The cutoff wavevector is chosen as

$$k_c = k_F / \sqrt{A}. \quad (15)$$

In previous applications of this kernel,^{30,31} the coefficient A defined by Eq. (10) was replaced by $1/4$, corresponding to

omitting the correlation contribution. In this work, we shall refer to this exchange-only kernel as the rALDA kernel f_{xc}^{rALDA} . The special label f_{xc}^{rALDAc} (rALDAc) refers to the kernel calculated including both the exchange and correlation contributions in Eq. (10). We note that the rALDAc kernel coincides with that of Ref. 61 with $B = 1$ and $C = 0$.

f_{xc}^{rALDAc} obeys the exact $k \rightarrow 0, \omega = 0$ limit for the HEG (Eq. (9)). Furthermore, both f_{xc}^{rALDAc} and f_{xc}^{rALDA} mimic the HEG kernel⁶⁴ in displaying small variation for wavevectors below $\sim 2k_F$. At larger wavevectors, both kernels correspond exactly to the Coulomb interaction with opposite sign, such that the corresponding Hartree-XC kernels f_{Hxc} vanish for $k > k_c$. In real space, the kernel has the form

$$f_{xc}^{\text{rALDA}}(n, R) = -\frac{1}{R} \left[1 - \frac{2}{\pi} \left(\int_0^{k_c R} \frac{\sin x}{x} dx - \frac{[\sin(k_c R) - k_c R \cos(k_c R)]}{(k_c R)^2} \right) \right] \quad (16)$$

with the Fourier transform of the Heaviside functions leading to decaying oscillations [Fig. 1(b)]. At small R , the XC-kernel diverges as $-1/R$, yielding a Hartree-XC kernel which is finite at the origin.³⁰

2. The CDOP kernel

The kernel introduced by CDOP in Ref. 17 has the form

$$f_{xc}^{\text{CDOP}}(n, k) = - \left[\frac{4\pi\alpha}{k_F^2} \left(\frac{k}{k_F} \right)^2 e^{-\beta(k/k_F)^2} + \frac{4\pi B}{k_F^2} \frac{1}{[g + (k/k_F)^2]} + \frac{4\pi C}{k_F^2} \right], \quad (17)$$

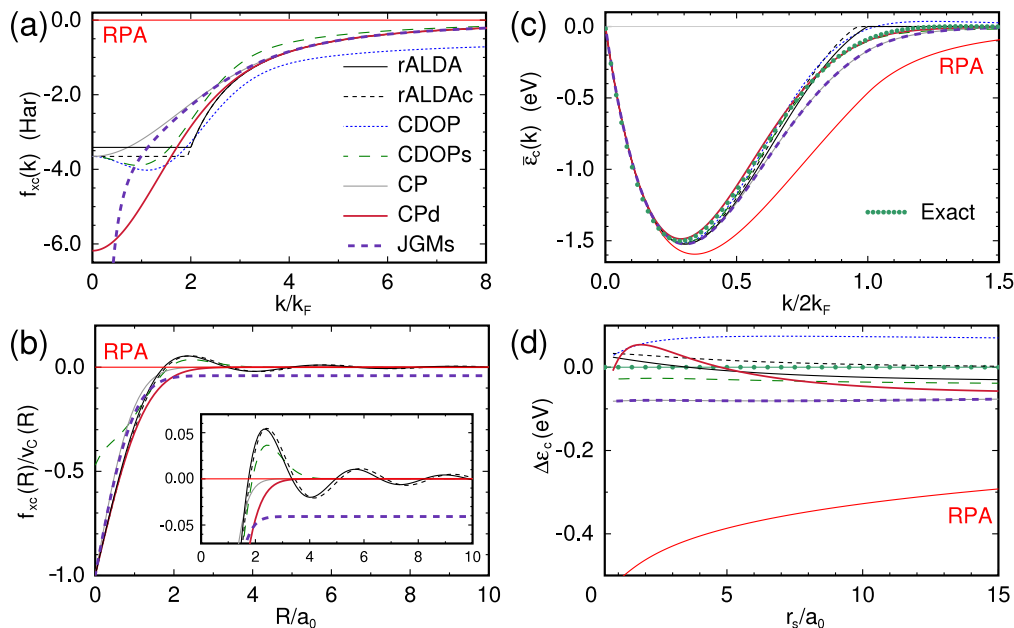


FIG. 1. Comparison of model HEG XC-kernels, plotted in (a) reciprocal and (b) real space for $r_s = 2$. In (b), the XC kernels are divided by the Coulomb interaction v_c , and the inset provides a zoomed image close to $f_{xc} = 0$. Apart from the JGMs, all the XC-kernels are short-range, while (apart from CDOPs) at small R , the XC-kernels cancel the Coulomb interaction such that f_{Hxc} vanishes. We have omitted the CDOP kernel in (b), since it matches CDOPs apart from a δ -function at $R = 0$ (Eq. (18)). The CPd kernel was evaluated at an energy of 2 Hartrees and the JGMs kernel at a band gap of 3.4 eV. In (c), we plot the wavevector-resolved correlation energy (Eq. (29)) at $r_s = 4$ compared to the exact¹⁵ result obtained from the parameterization of the correlation hole given in Refs. 67 and 68. In (d), we plot the difference in calculated correlation energies with a parameterization⁶³ of Monte Carlo calculations⁶⁹ of ϵ_c .

where $g = B/(A - C)$, and α and β are density-dependent fitting parameters chosen to best reproduce the local field factor $G(k, \omega = 0)$ obtained from the quantum Monte Carlo calculations of Ref. 64.

Uniquely among the kernels considered here, the CDOP kernel obeys both the $k \rightarrow 0$ and $k \rightarrow \infty$ limits of the HEG at $\omega = 0$, Eqs. (9) and (11). However as noted above, the short-wavelength C term causes the pair-distribution function to diverge.²⁹ In Ref. 29, a simplified kernel which avoids this divergence was obtained from Eq. (17) by setting $C = 0$. We shall also investigate this kernel in this work, labeled CDOPs (f_{xc}^{CDOPs}).

The real-space form of the CDOP kernel is

$$f_{xc}^{\text{CDOP}}(n, R) = -\frac{1}{R} B e^{-\sqrt{g} k_F R} - \frac{4\pi C}{k_F^2} \delta(R) + \frac{\alpha k_F}{4\pi^2 \beta} \left(\frac{\pi}{\beta} \right)^{\frac{3}{2}} \left[\frac{k_F^2 R^2}{2\beta} - 3 \right] e^{-k_F^2 R^2 / 4\beta}. \quad (18)$$

We note that the C term in Eq. (17) produces a δ -function in real-space, while for small R (excluding the δ -function), the XC-kernel diverges as $-B/R$, such that the Hartree-XC kernel is still divergent as $(1 - B)/R$.

3. The Constantin and Pitarke (CP) kernel

A kernel with a simpler functional form was introduced by CP in Ref. 16,

$$f_{xc}^{\text{CP}}(n, k) = -\left[\frac{4\pi}{k^2} (1 - e^{-\kappa_0 k^2}) \right]. \quad (19)$$

Here $\kappa_0 = A/k_F^2$, which ensures that the HEG $k \rightarrow 0$, $\omega = 0$ limit is satisfied. Like the rALDA kernels, at large wavevectors $f_{xc}^{\text{CP}}(k)$ cancels the Coulomb interaction so that f_{Hxc} vanishes. The CP kernel possesses a compact form in real space in terms of the error function,

$$f_{xc}^{\text{CP}}(n, R) = -\frac{1}{R} \left[1 - \text{erf} \left(\frac{R}{\sqrt{4\kappa_0}} \right) \right]. \quad (20)$$

As $R \rightarrow 0$, f_{xc}^{CP} diverges as $-1/R$ and thus yields a finite Hartree-XC kernel in this limit.

4. The CPd dynamical kernel

With its simple form, the CP kernel is an ideal starting point to explore more complex aspects of f_{xc} , such as its frequency dependence. In Ref. 16, a dynamical kernel was introduced (CPd) by replacing κ_0 appearing in Eq. (19) with κ_ω , i.e.,

$$f_{xc}^{\text{CPd}}(n, k, \omega) = -\left[\frac{4\pi}{k^2} (1 - e^{-\kappa_\omega k^2}) \right], \quad (21)$$

where for imaginary frequency $\omega = is$,

$$\kappa_\omega = \kappa_0 \frac{1 + as + cs^2}{1 + s^2}. \quad (22)$$

In Ref. 16, the coefficient $c = D/A$ was chosen to correctly reproduce the $k \rightarrow 0$, $\omega \rightarrow \infty$ limit of the HEG (Eq. (12)), while the relation $a = 6\sqrt{c}$ was found to give a good fit to the correlation energy calculated for the HEG using f_{xc}^{CPd} . We note that the CPd kernel varies non-monotonically with frequency in the $k \rightarrow 0$ limit.¹⁶

5. The simplified “jellium with gap” (JGMs) kernel

The limits of the exact kernel discussed in Sec. II C 2 were derived for the HEG, which is metallic. However, the XC-kernel of a periodic *insulator* is known to behave differently, diverging $\propto 1/k^2$ in the $k \rightarrow 0$ limit.^{36,37} This limit has been found to play an essential role in the TD-DFT calculation of excitonic effects in optical spectra, leading to the development of kernels which exhibit the same $1/k^2$ divergence.^{38,70,71} Here, we focus on the JGM kernel of Ref. 38, which has the useful property of reducing to a model HEG kernel¹⁶ when applied to a metallic system.

The JGM kernel of Ref. 38 was derived based on two steps. First, the theoretical arguments of Ref. 72 were used to connect the $k \rightarrow 0$ limit of f_{xc} to ϵ , the dielectric function, as $f_{xc}(k \rightarrow 0) = -4\pi/[k^2(\epsilon - 1)]$ (a similar relation was found empirically in Ref. 70). Then, the model dielectric function of Ref. 73 was used to relate ϵ to the band gap of the material E_g , as $\epsilon - 1 = 4\pi n/E_g^2$. The same power dependence may be found for other model dielectric functions, e.g., the Penn model,⁷⁴ and essentially follows from the f -sum rule. Combining these relations places a requirement on the model kernel that it diverges as $-\alpha/k^2$ in the small k limit, where $\alpha \rightarrow E_g^2/n$.

In Ref. 38, the JGM kernel was constructed to satisfy this divergence, based on a modified CP kernel introduced in Ref. 16. Following their approach, starting from the unmodified CP kernel f_{xc}^{CP} , we introduce a simplified JGM (JGMs) kernel f_{xc}^{JGMs} for a system with a gap as

$$f_{xc}^{\text{JGMs}}(n, k, E_g) = -\left[\frac{4\pi}{k^2} (1 - e^{-\kappa_0 k^2} e^{-E_g^2/(4\pi n)}) \right]. \quad (23)$$

f_{xc}^{JGMs} has many of the properties of the JGM kernel introduced in Ref. 38. For systems with a band gap, the XC-kernel diverges as $-\alpha/k^2$ at small k . For $E_g = 0$, f_{xc}^{JGMs} reduces to f_{xc}^{CP} (Eq. (19)), while for $E_g \rightarrow \infty$, $f_{xc}^{\text{JGMs}} \rightarrow -v_c$, yielding a vanishing correlation energy. Indeed, the JGMs kernel differs only from the JGM kernel in its behavior at large k , with the JGM kernel correctly reproducing the $\omega = 0$ limit of the HEG for $E_g = 0$ (Eq. (11)); concomitantly the JGM kernel has a diverging pair-distribution function. By introducing the JGMs kernel, we can study the effect of the $-\alpha/k^2$ divergence without any additional complications potentially arising from a badly behaved pair-distribution function.

The real-space form of the JGMs kernel is

$$f_{xc}^{\text{JGMs}}(R) = -\frac{1}{R} \left[1 - e^{-E_g^2/(4\pi n)} \text{erf} \left(\frac{R}{\sqrt{4\kappa_0}} \right) \right]. \quad (24)$$

Equation (24) and Fig. 1(b) emphasize a unique property of the JGMs kernel: it is long range. As a result, at large R , the Hartree-XC kernel does not reduce to the bare Coulomb kernel but rather to an interaction weakened by a factor $\exp[-E_g^2/(4\pi n)]$.

6. Coupling-constant dependence

Evaluating the integral over λ in Eq. (1) requires the f_{xc} kernel at an arbitrary coupling strength. We use the analysis of Ref. 15 to link f_{xc}^λ to the fully interacting kernel through the

relation

$$f_{xc}^\lambda(n, k, \omega) = \lambda^{-1} f_{xc}(n/\lambda^3, k/\lambda, \omega/\lambda^2). \quad (25)$$

The scaling of the density can be equivalently stated as λr_s or k_F/λ . The (exchange-only) rALDA XC-kernel has the useful property that $f_{xc}^{\text{rALDA}, \lambda} = \lambda f_{xc}^{\text{rALDA}}$.

For the JGMs kernel, we have an additional parameter E_g . For simplicity, we employ a scaling

$$f_{xc}^{\text{JGMs}, \lambda}(n, k, E_g) = \lambda^{-1} f_{xc}^{\text{JGMs}}(n/\lambda^3, k/\lambda, E_g/\lambda^{1.5}), \quad (26)$$

equivalent to treating E_g^2/n independent of λ .

7. Analogy with range-separated RPA

It is interesting to draw comparisons with RPA methods based on the concept of range-separation.^{75–77} First, we trivially relabel the Hartree-XC kernel as an effective interaction v_{eff} , i.e., $v_{\text{eff}} = v_c + f_{xc}$, noting from Fig. 1(b) that for most of the kernels v_{eff} goes to zero at $R \rightarrow 0$ and tends to the full Coulomb interaction at large R . Now, specializing to a static model XC-kernel which scales linearly with coupling constant, $f_{xc}^\lambda(\mathbf{q}) = \lambda f_{xc}(\mathbf{q})$, we can partition the correlation energy in Eq. (1) into two contributions $E_c = E_c^{\text{LR}} + E_c^{\text{SR}}$, with

$$E_c^{\text{LR}} = \frac{1}{2\pi} \sum_{\mathbf{q}} \int_0^\infty ds \text{Tr} [\ln \{1 - v_{\text{eff}}(\mathbf{q}) \chi_{\text{KS}}(\mathbf{q}, is)\} + v_{\text{eff}}(\mathbf{q}) \chi_{\text{KS}}(\mathbf{q}, is)], \quad (27)$$

$$E_c^{\text{SR}} = \frac{1}{2\pi} \sum_{\mathbf{q}} \int_0^1 d\lambda \int_0^\infty ds \times \text{Tr} [f_{xc}(\mathbf{q})(\chi^\lambda(\mathbf{q}, is) - \chi_{\text{KS}}(\mathbf{q}, is))]. \quad (28)$$

Equation (27) matches the RPA expression for the correlation energy (Eq. (7)) with v_c replaced with v_{eff} . Similarly, Eq. (28) matches the expression for the full correlation energy (Eq. (1)) with v_c replaced by $-f_{xc}$, which is generally a short-ranged interaction.

We can focus further on the specific example of the CP XC-kernel (Eq. (19)), noting that this kernel can be linearized in λ by neglecting the correlation contribution to A in Eq. (10). Then, $v_{\text{eff}} = \text{erf}(\mu R)/R$, with the “range-separation parameter” μ determined by the density through $\mu = k_F \sim 1.9/r_s$. This effective interaction is often found in the range-separated RPA⁷⁵ with μ of order unity.

We stress that Eqs. (27) and (28) are exact for any kernel which obeys $f_{xc}^\lambda(\mathbf{q}) = \lambda f_{xc}(\mathbf{q})$. Since most of the XC-kernels under study here do not obey this relation, we have not explored Eqs. (27) and (28) further in this work. However for XC-kernels linear in λ (e.g., the rALDA), there may be a computational advantage in calculating E_c^{LR} and E_c^{SR} separately. E_c^{LR} requires only χ_{KS} and not χ^λ , so for a given kernel, it can be obtained at exactly the same cost as the RPA correlation energy. In fact, since the effective interaction v_{eff} generally vanishes at large wavevectors, E_c^{LR} can be expected to avoid the basis-set convergence problems of the RPA recently highlighted in Ref. 78. Meanwhile, it may be possible to exploit the short-range character of f_{xc} to reduce the computational cost of calculating E_c^{SR} from Eq. (28).

E. Calculating HEG correlation energies

A standard test of model HEG kernels is to calculate the correlation energy per electron ε_c from Eqs. (1) and (8). For a given density r_s , ε_c can be resolved as an integral over k as¹⁵

$$\varepsilon_c = \int_0^\infty \bar{\varepsilon}_c(k) d(k/2k_F). \quad (29)$$

The quantity $\bar{\varepsilon}_c(k)$ can be compared to the Fourier transform of a suitable parameterization of the “exact” correlation hole obtained from Monte Carlo calculations.^{15,67,68} Alternatively, one can compute ε_c over a range of densities and compare to the parameterized result.⁶³ These comparisons are made in Figs. 1(c) and 1(d), respectively.

The HEG analysis has been performed a number of times^{15,16,30} so we only summarize the key points. The RPA correlation is too negative, while including any of the XC-kernels brings ε_c to within 0.1 eV of the exact result. Considering the wavevector decomposition in Fig. 1(c), we find that the dynamical CPd kernel provides the best description of the correlation hole at this density ($r_s = 4$), but below $\sim 1.5k_F$, there is very little difference between any of the XC-kernels and the exact result. Indeed, the ALDA (not shown) also provides a good description of the correlation hole at these wavevectors. At larger wavevectors, differences begin to emerge between the kernels, with the CP kernel becoming too negative, the CPd and CDOPs kernels closely following the exact result, and the other kernels too positive. The rALDA kernels are abruptly cut off at $\bar{\varepsilon}_c(k) = 0$, while the CDOP kernel acquires a slowly decaying positive contribution. The latter behavior is observed to a greater extent in the ALDA and originates from the locality of the kernels.^{15,30}

Over the full range of densities [Fig. 1(d)], we find that the calculated correlation energy is slightly too positive with the CDOP kernel and too negative with the CP and CDOPs kernels. Interestingly, CDOPs is closer to the exact result than CDOP, illustrating that removing the part of the CDOP kernel which causes the pair-distribution function to diverge²⁹ slightly improves the correlation energy. The rALDA kernels fall closest to the exact result across a wide range of densities, and the CPd kernel also provides a good description of the correlation energy. Comparing rALDA and rALDAc, we see that removing the correlation contribution from A in Eq. (10) decreases the correlation energy per electron by less than ~ 0.02 eV across a range of densities.

F. Coupling-constant averaged pair-distribution function

Clearly, all of the considered kernels greatly improve the correlation energy of the HEG compared to the RPA. The common characteristics shared by the kernels are that they satisfy the exact $k \rightarrow 0$, $\omega = 0$ limit of the HEG (except the rALDA, which neglects the correlation contribution in Eq. (10)) and that they decay for wavevectors above $2k_F$. This decay is essential to an accurate description of the energetics of the HEG, with the ALDA (which does not decay at large k), yielding a correlation energy which is too positive.³⁰ However, the fact that we only observe small variations between the

kernels considered in Fig. 1(d) indicates that the precise form of this decay is less important.

It is however interesting to consider the coupling-constant averaged pair-distribution function $\bar{g}_c(R)$,⁶⁷ obtained as the Fourier transform of $\bar{\epsilon}_c(k)$ multiplied by $\pi/[2nk_F]$.¹⁵ The pair-distribution function $g_c(R)$ is obtained from the derivative of $\bar{g}_c(R)$ with respect to r_s , and the exact g_c and \bar{g}_c both satisfy cusp conditions such that their slopes at $R = 0$ are generally nonzero.^{65,67} Concentrating on $\bar{g}_c(R)$, we note that in order to describe a cusp in real space, we require Fourier components [i.e., nonzero $\bar{\epsilon}_c(k)$] at large k . Indeed, the analysis of Ref. 65 finds that a frequency-independent kernel must decay as $-\gamma/k^2$, where $\gamma < 4\pi$, i.e., the Hartree-XC kernel retains a $1/k^2$ term at large k . By considering Fig. 1(a), we see that the rALDA, CP, and CPd kernels all decay as $-4\pi/k^2$ such that their Hartree-XC kernels vanish, so that $\bar{\epsilon}_c(k)$ also quickly tends to zero at large wavevectors [Fig. 1(c)]. Thus, these kernels cannot describe the cusp.

To illustrate this behavior, in Fig. 2, we plot $\bar{g}_c(R)$ calculated at $r_s = 2$ for the different kernels, compared to the RPA and to the parameterization of Refs. 67 and 68. It is clear that the coupling-constant averaged pair-distribution functions calculated for the rALDA, CP, and CPd kernels are far softer than those calculated for the RPA and CDOPs, whose Hartree-XC kernels decay $\propto 1/k^2$. Meanwhile as noted above, the local C term of the CDOP kernel causes a divergence in $\bar{g}_c(R)$.

The slope of coupling-constant averaged pair-distribution function calculated in the RPA is too steep, while it is improved for CDOPs. In Ref. 29, it was also found that $g_c(R)$ calculated for CDOPs agreed well with the exact result. The good performance of the CDOPs kernel for calculations of the pair-distribution function might have been anticipated from the fact that the coefficient B appearing in Eq. (17) itself is determined from $g(R = 0)$.⁶⁴ The above analysis illustrates how the precise large- k behavior of a kernel affects its description of the cusp

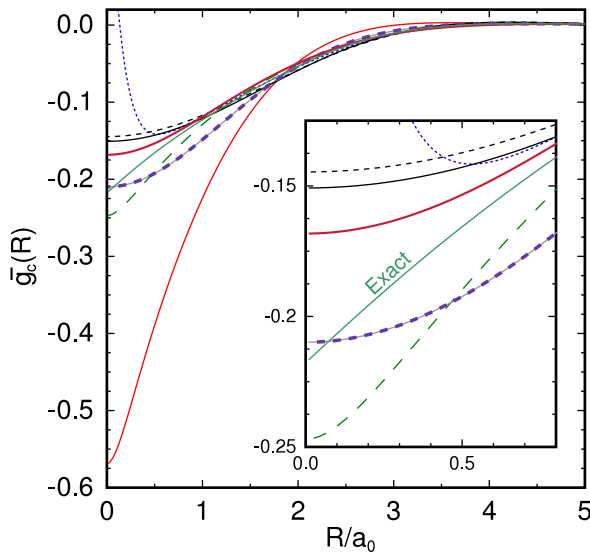


FIG. 2. Coupling-constant averaged pair-distribution function $\bar{g}_c(R)$ calculated at $r_s = 2$ for the model HEG XC-kernels (see Fig. 1 for color code), compared to the “exact” parameterization given in Eq. (36) of Ref. 67 (see also Ref. 68). The inset shows the zoomed region around $\bar{g}_c(R = 0)$.

of $g_c(R)$, despite playing a lesser role in the calculation of energetics.

G. Applying HEG kernels to inhomogeneous systems

In order to calculate the correlation energy of an inhomogeneous system through Eq. (1), we require f_{xc} evaluated in a plane-wave basis, which in general is constructed from the real-space kernel through

$$f_{xc}^{GG'}(\mathbf{q}, \omega) = \frac{1}{V} \int_V d\mathbf{r} \int_V d\mathbf{r}' e^{-i(\mathbf{q}+\mathbf{G})\cdot\mathbf{r}} \times f_{xc}(\mathbf{r}, \mathbf{r}', \omega) e^{i(\mathbf{q}+\mathbf{G}')\cdot\mathbf{r}'}, \quad (30)$$

where V is the volume of the entire crystal, consisting of N_q replicas of the unit cell of volume Ω . The question is how to incorporate into this formalism, a model (m) kernel which has the form $f_{xc}^m(n, k, \omega)$ or $f_{xc}^m(n, |\mathbf{r} - \mathbf{r}'|, \omega)$. In the case that the system is homogeneous ($n(\mathbf{r}) = n$), we simply make the substitution $f_{xc}(\mathbf{r}, \mathbf{r}', \omega) \rightarrow f_{xc}^m(n, |\mathbf{r} - \mathbf{r}'|, \omega)$ to get a diagonal kernel,

$$f_{xc}^{\text{hom } GG'}(\mathbf{q}, \omega) = \delta_{\mathbf{G}\mathbf{G}'} f_{xc}^m(n, |\mathbf{q} + \mathbf{G}|, \omega). \quad (31)$$

Alternatively, if the model kernel is fully local (independent of k , e.g., the ALDA), it is natural to choose the local density to construct the kernel and obtain

$$f_{xc}^{\text{loc } GG'}(\mathbf{q}, \omega) = \frac{1}{\Omega} \int_{\Omega} d\mathbf{r} e^{-i(\mathbf{G}-\mathbf{G}')\cdot\mathbf{r}} f_{xc}^m(n(\mathbf{r}), \omega). \quad (32)$$

However for nonlocal kernels and inhomogeneous systems, it is not obvious how one should construct $f_{xc}(\mathbf{r}, \mathbf{r}', \omega)$, except for two requirements. First, an arbitrary model kernel should be symmetric in \mathbf{r} and \mathbf{r}' ,⁷⁹

$$f_{xc}(\mathbf{r}, \mathbf{r}', \omega) = f_{xc}(\mathbf{r}', \mathbf{r}, \omega). \quad (33)$$

Second, for the JGMs kernel, we require that in the $q \rightarrow 0$ limit, the head of f_{xc} (i.e., $\mathbf{G} = \mathbf{G}' = 0$) diverges as $1/q^2$ while the wings ($\mathbf{G} \neq \mathbf{G}' = 0$) diverge no faster than $1/q$ (Ref. 37). As shown below, this second requirement turns out to exclude previous schemes used in ACFD-DFT calculations, which we now briefly review.

1. Density symmetrization

A symmetric kernel can be obtained by making the following substitution into Eq. (30):

$$f_{xc}(\mathbf{r}, \mathbf{r}', \omega) \rightarrow f_{xc}^m(\mathcal{S}[n], |\mathbf{r} - \mathbf{r}'|, \omega). \quad (34)$$

Here, \mathcal{S} is a functional of the density symmetric in \mathbf{r} and \mathbf{r}' , whose possible forms span a wide range of complexity.^{80,81} References 22 and 31 take a two-point average, $\mathcal{S}[n] = 1/2[n(\mathbf{r}) + n(\mathbf{r}')]$, which has an intuitive interpretation.

A disadvantage of the symmetrization in Eq. (34) is that in order to evaluate Eq. (30), it is necessary to work with a real-space representation of the kernel and perform an integration over the entire volume of the crystal. For short-range kernels, this integral can be converged by sampling over a number of unit cells,³¹ but for a long-range kernel like f_{xc}^{JGMs} [decaying as $-\alpha/(4\pi R)$], the required sampling might be prohibitively large. Also, since the kernel is constructed in real space, it is

not obvious how to control the $1/q$ divergences of the JGMs kernel in reciprocal space. Finally, we note that the $1/R$ real-space divergence of the kernels leads to slow convergence with the real-space grid used to evaluate the integral in Eq. (30).³¹

2. Kernel symmetrization

An alternative approach followed in Ref. 29 is to start from a nonsymmetric form of f_{xc} , which we label f_{xc}^{NS} ,

$$f_{xc}^{NS}(\mathbf{r}, \mathbf{r}', \omega) = f_{xc}^m(n(\mathbf{r}), |\mathbf{r} - \mathbf{r}'|, \omega). \quad (35)$$

Inserting f_{xc}^{NS} into Eq. (30) gives

$$f_{xc}^{NS,GG'}(\mathbf{q}, \omega) = \frac{1}{\Omega} \int_{\Omega} d\mathbf{r} e^{-i(\mathbf{G}-\mathbf{G}')\cdot\mathbf{r}} f_{xc}^m(n(\mathbf{r}), |\mathbf{q} + \mathbf{G}'|, \omega). \quad (36)$$

A symmetric kernel can then be obtained by averaging $f_{xc}^{NS,GG'}$ with its Hermitian conjugate, i.e.,

$$f_{xc}^{S,GG'}(\mathbf{q}, \omega) = \frac{1}{2} \left(f_{xc}^{NS,GG'}(\mathbf{q}, \omega) + [f_{xc}^{NS,G'G}(\mathbf{q}, \omega)]^* \right). \quad (37)$$

This procedure can be seen equivalently²⁹ as inserting the symmetric combination $1/2[f_{xc}^{NS}(\mathbf{r}, \mathbf{r}', \omega) + f_{xc}^{NS}(\mathbf{r}', \mathbf{r}, \omega)]$ into Eq. (30), and therefore corresponds to a two-point average of the kernel; in the case that the kernel is linear in density, this scheme is equivalent to averaging the density. Equation (36) has the computational advantages that the integral is over a single unit cell and requires only that the density (and not the kernel) is represented on the real-space grid. However, considering the JGMs XC-kernel, upon inserting Eq. (23) into Eq. (36) and performing the average of Eq. (37), we are left with a matrix whose wings diverge $\propto 1/q^2$ as $q \rightarrow 0$, not $1/q$ as required. Therefore, Eq. (37) is unsuitable for the current study.

3. Wavevector symmetrization

In order to correctly deal with the JGMs kernel while retaining some of the computational advantages of Eq. (36), we follow the approach of Ref. 38 and symmetrize the wavevector appearing in the right hand side of Eq. (36) with the substitution $|\mathbf{q} + \mathbf{G}'| \rightarrow \sqrt{|\mathbf{q} + \mathbf{G}'||\mathbf{q} + \mathbf{G}|}$,

$$f_{xc}^{GG'}(\mathbf{q}, \omega) = \frac{1}{\Omega} \int_{\Omega} d\mathbf{r} e^{-i(\mathbf{G}-\mathbf{G}')\cdot\mathbf{r}} \times f_{xc}^m \left(n(\mathbf{r}), \sqrt{|\mathbf{q} + \mathbf{G}'||\mathbf{q} + \mathbf{G}|}, \omega \right). \quad (38)$$

Like Eq. (36), Eq. (38) requires the integral over the unit cell only and deals with the reciprocal-space form of the kernels. Using Eq. (38) to construct the JGMs kernel yields a matrix whose head and wings diverge in the $q \rightarrow 0$ limit as $1/q^2$ or $1/q$, as required, while the hermiticity of $f_{xc}^{GG'}(\mathbf{q}, \omega)$ automatically satisfies the symmetry requirement (Eq. (33)). Trivially, the averaging scheme will reproduce Eqs. (31) and (32) when applied to systems with a homogeneous density or a local kernel, and furthermore, the diagonal ($\mathbf{G} = \mathbf{G}'$) elements coincide with those calculated with the two-point average of the kernel, Eq. (37).

Since this work is concerned with the comparison of a large number of kernels, we have elected to use Eq. (38) on the grounds that it is relatively efficient and can deal with the divergences in the JGMs kernel correctly. However, the physical interpretation of the off-diagonal elements arising from the wavevector-symmetrization is not transparent. Although a two-point scheme also suffers from limitations (e.g., the two-point kernel has no knowledge of the medium lying between \mathbf{r} and \mathbf{r}'), it still remains a more intuitive procedure. The fact that we have to invoke an averaging scheme at all is an undesirable consequence of using HEG kernels to describe inhomogeneous systems. In reality, the use of different schemes can only be justified through testing and comparison with experiments or other calculations, such as that performed in Refs. 29–32 and here.

H. Computational details

All calculations in this work were performed using the GPAW code.⁸² The Kohn-Sham states and energies used to construct the response function (Eq. (6)) were calculated using the local-density approximation to DFT^{1,2,63} within the projector-augmented wave (PAW) framework.⁸³ We used $6 \times 6 \times 6$ and $12 \times 12 \times 12$ unshifted Monkhorst-Pack⁸⁴ meshes to sample the Brillouin zone for insulators and metals, respectively, and constructed the occupation factors for each Kohn-Sham state using a Fermi-Dirac distribution function of width 0.01 eV. For H, He, and H₂, we used a simulation cell of $6 \times 6 \times 7 \text{ \AA}^3$ and Γ -point sampling.

When calculating E_c , the wavefunctions were expanded in a plane-wave basis set up to a maximum kinetic energy of 600 eV. Following previous studies,^{31,46} we used the frozen-core approximation but included semicore states for some elements.⁸⁵ We note that norm-conservation was not enforced in the generation of our PAW potentials, while it is reported in Ref. 78 that including norm-conservation might increase the magnitude of the RPA correlation energy and decrease the calculated lattice constants for certain materials. As a result, some care should be taken in making comparisons to experiment, although we expect calculations including the XC-kernel to be less sensitive to this convergence issue (Sec. II D 7).

For the matrices representing the response function and kernel, we used a lower plane-wave cutoff E_{cut} of 400 eV (300 eV for Na and H₂), and a \mathbf{q} grid matching the Brillouin zone sampling of the ground-state calculation. We truncated the sum-over-states appearing in Eq. (6) at a number of bands equal to the number of plane waves describing the response function, e.g. ~ 700 for Si. Within this approximation, the following extrapolation scheme is commonly used for the RPA correlation energy:^{46,78}

$$E_c^{\text{RPA}}(E_{\text{cut}}) \sim E_c^{\text{RPA}}(E_{\text{cut}} \rightarrow \infty) + K E_{\text{cut}}^{-3/2}. \quad (39)$$

In Ref. 31, it was proposed that the same expression can be applied to the correlation energy calculated with the rALDA kernel. We have tested this expression for each of the kernels in Sec. II D for a set of 10 materials (see Sec. III A). As an example, in Fig. 3, we plot the correlation energy per electron calculated for MgO as a function of $E_{\text{cut}}^{-3/2}$. As demonstrated by the straight lines, Eq. (39) apparently gives a good description

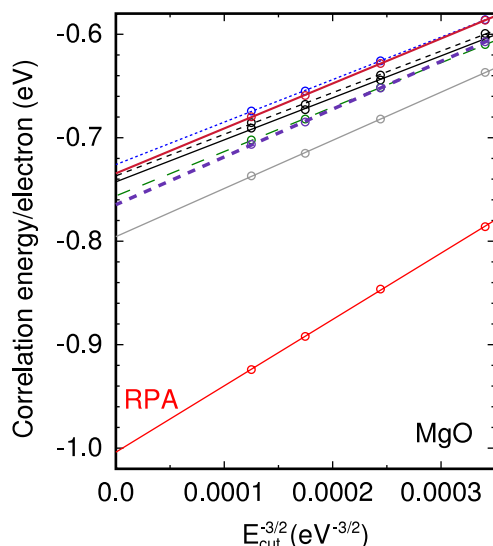


FIG. 3. The correlation energy E_c evaluated per electron for MgO at a lattice constant of 4.23 Å, using different approximations for the XC-kernel (see Fig. 1 for the color code). E_{cut} is the plane-wave cutoff used for the matrices representing the response function and XC-kernel. The circles represent calculated data points, and the lines are fits from Eq. (39).

of the correlation energy calculated for $E_{\text{cut}} > 200$ eV for all of the kernels. We have observed the same behavior across the combinations of materials and kernels. Therefore in order to facilitate comparison across the entire test set, we will apply Eq. (39) for all XC-kernels. We point out that the correlation energy tends to converge faster (shallower lines in Fig. 3) when a nonzero f_{xc} is used, and for calculating structural properties, the extrapolation is often unnecessary.

Constructing the XC-kernel with Eq. (38) is not straightforward due to the dual dependence on \mathbf{G} and \mathbf{G}' . Our current implementation distributes the rows of the f_{xc} matrix among processors before evaluating the integral in Eq. (38). In the future, it may be appropriate to improve performance through an interpolation scheme, as for Refs. 29 and 86. On the other hand, for the systems studied here, the time taken to construct the kernel is small compared to that spent constructing the response function χ_{KS} and inverting Eq. (3). When constructing the kernel, we use the PAW all-electron density to be consistent with previous work.³¹ The $1/q^2$ divergence of the Coulomb interaction and JGMs kernel was treated within the scheme described in Ref. 41.

Having obtained χ^λ , we evaluated Eq. (1) by numerical (Gauss-Legendre) integration over the coupling constant ($N_\lambda = 8$ points) and frequency ($N_\omega = 16$ points, using a logarithmic mesh).⁴⁹ By virtue of the scaling relation (Eq. (25)), we must construct the rALDA kernel once, a general static kernel N_λ times and a dynamical kernel $N_\lambda N_\omega$ times; hence, there is a prefactor of ~ 100 applied to computing f_{xc}^{CPd} compared to f_{xc}^{rALDA} .

To calculate structural properties, we evaluated the total energy $(E_{\text{Tot}}^{\text{LDA}} - E_{xc}^{\text{LDA}}) + E_x + E_c$ for seven lattice constants centered around the experimental value and fit the values to the Birch-Murnaghan equation of state.⁸⁷ We used higher plane-wave cutoffs of 800 eV (900 eV for MgO, LiCl, and LiF) to evaluate the LDA energies and E_x , and used a denser sam-

pling of the Brillouin zone combined with the Wigner-Seitz truncation scheme described in Ref. 88 to calculate E_x . We typically obtain converged exchange energies for insulators with a sampling of $10 \times 10 \times 10$, while metals require a denser sampling⁸⁸ (e.g. $20 \times 20 \times 20$). Since the bulk modulus is constructed from derivatives of the energy, it is rather prone to numerical error, to the extent that different code implementations of the same method can yield different results.⁸⁹ In this respect, one should attach more significance to the calculated lattice constants than bulk moduli, since the former are more robust quantities. However even for the bulk moduli, one expects a reduction in error when comparing different XC-kernels within the same computational framework.

III. RESULTS AND DISCUSSION

A. Lattice constants and bulk moduli

We have selected a test set of 10 materials, consisting of 3 tetrahedrally bonded semiconductors (diamond C, Si, and SiC), 3 ionic compounds (MgO, LiCl and LiF) and 4 metals (Al, Na, Cu, and Pd). For each material, we used the XC-kernels introduced in Sec. II D to calculate the lattice constant and bulk modulus. Here, we compare these results to those obtained from DFT (in the LDA or from the generalized-gradient PBE functional⁹⁰), the RPA, and to the experimental values tabulated in Ref. 46.

1. General trends

Figure 4 shows the lattice constants and bulk moduli calculated for C, MgO, and Al as a function of $E_{\text{cut}}^{-3/2}$, a quantity inversely proportional to the number of plane-waves describing the response function χ_{KS} and XC-kernel f_{xc} (cf. Fig. 3). The quantities at $E_{\text{cut}}^{-3/2} = 0$ were calculated from E_c extrapolated to infinite E_{cut} using Eq. (39). We also show the values obtained from the LDA and experiment as horizontal lines.

There are three key observations to be made from Fig. 4. First, for non-metallic systems, the rALDA, rALDac, CDOPs, and CP kernels yield almost identical results, which in turn are very similar to the RPA. Second, the JGMs, CPd, and the CDOP kernels (which, respectively, are long-range, dynamical or have a local term) display distinct behavior. For instance, the JGMs kernel predicts smaller lattice constants and larger bulk moduli than the other XC-kernels. Finally, all of the XC-kernels show faster convergence with respect to E_{cut} compared to the RPA, as found for the correlation energy (Fig. 3).

Keeping the above points in mind, we extend this analysis to the full test set and consider each kernel in turn. The entire dataset is given in Fig. 5 and Table I.

2. LDA, PBE, and RPA

The LDA typically underestimates lattice constants and overestimates bulk moduli, while PBE displays opposite behavior. For tetrahedral semiconductors, the LDA is difficult to beat and is by far the most computationally efficient scheme. Using exact exchange and the RPA correlation energy yields improved bulk moduli and lattice constants (e.g., a mean

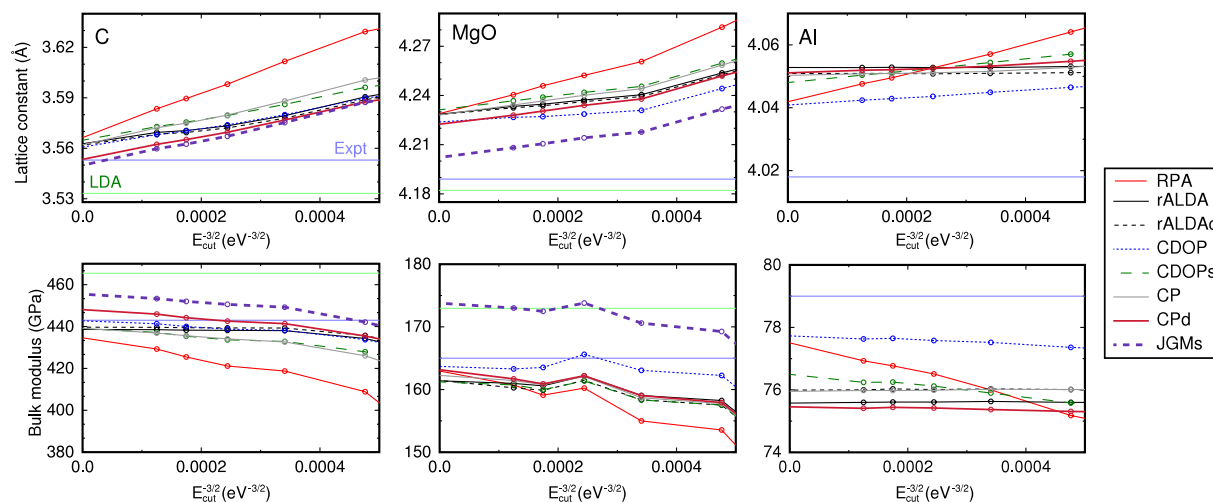


FIG. 4. Lattice constants and bulk moduli calculated with different XC-kernels for C, MgO, and Al, vs $E_{\text{cut}}^{-3/2}$, where E_{cut} is the plane-wave cutoff of the response function and XC-kernel matrices. The green and blue horizontal lines give the values calculated with the LDA and obtained from experiment, respectively, where the experimental data were tabulated in Ref. 46 (note the LDA lattice constant/bulk modulus for Al [3.99 Å/83 GPa] is off the scale). The values at infinite cutoff ($E_{\text{cut}}^{-3/2} = 0$) were calculated from the correlation energies extrapolated from Eq. (39).

absolute error in lattice constants of 0.6% compared to 1.2% for the LDA). Apart from Na, the calculated RPA lattice constants are larger than the experimental values, a result also found in Ref. 46.

3. rALDA and rALDAc

For the non-metallic systems, the rALDA and rALDAc kernels produce lattice constants and bulk moduli which are essentially indistinguishable from each other. In turn, these results are in close agreement with the RPA. For metals, one can identify differences between the kernels, although the magnitude of variation is still very small ($<0.1\%$). The close

agreement between rALDA and rALDAc confirms that the exchange contribution dominates in Eq. (10) and supports the use of the exchange-only rALDA kernel.

The rALDA kernels also display the fastest convergence with respect to E_{cut} . Recalling the form of the kernels (Eq. (14)), the components of f_{Hxc} are truncated for wavevectors exceeding the cutoff k_c . For a homogeneous system (Eq. (8)), for $k' > k_c$, the interacting and non-interacting response functions coincide and therefore the contribution to the correlation energy at these wavevectors vanishes. In inhomogeneous systems, high-density regions (large k_c) give terms that converge like the RPA, but the rALDA convergence is still superior after the kernel averaging procedure (Eq. (38)) is applied.

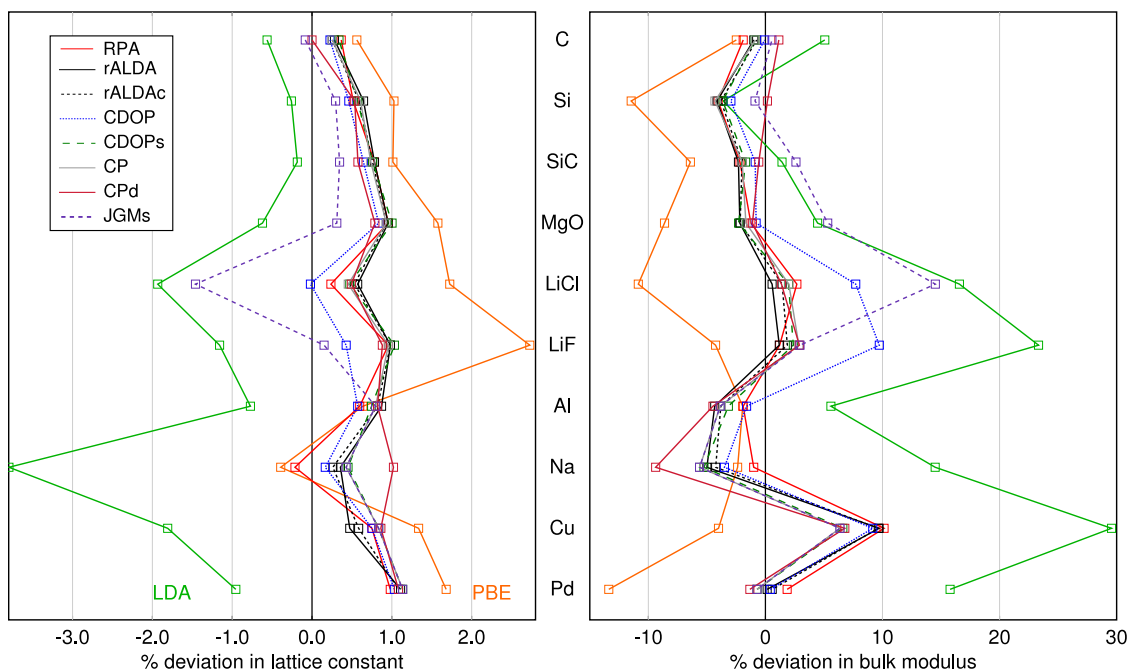


FIG. 5. Percentage deviation from experiment of calculated lattice constants and bulk moduli for the test set of 10 materials. The values used to construct the plots are presented in Table I. Each line corresponds to a different approximation for f_{xc} .

TABLE I. Lattice constants (in Å) and bulk moduli (GPa) calculated for the test set of 10 materials compared to the experimental data tabulated in Ref. 46. The results were calculated from correlation energies obtained by the extrapolation procedure of Eq. (39). The mean absolute error (M.A.E.) compared to experiment is shown in the final row. The experimental lattice constants were corrected for expansion due to zero-point motion; the bulk moduli have not been corrected. For comparison, the LDA and RPA calculations of Ref. 46 are also presented (note that these RPA calculations were performed on top of Kohn-Sham states obtained within the generalized-gradient approximation⁹⁰). The CP and JGMs kernels coincide for metallic systems.

	LDA	LDA ^a	PBE	RPA	RPA ^a	rALDA	rALDAc	CDOP	CDOPs	CP	CPd	JGMs	Expt.
C	3.533	3.534	3.573	3.566	3.572	3.563	3.562	3.561	3.565	3.562	3.553	3.550	3.553
Si	5.407	5.404	5.477	5.449	5.432	5.456	5.453	5.446	5.452	5.454	5.450	5.437	5.421
SiC	4.338	4.332	4.390	4.380	4.365	4.380	4.379	4.374	4.379	4.378	4.371	4.361	4.346
MgO	4.163	4.169	4.255	4.229	4.225	4.229	4.228	4.224	4.231	4.228	4.222	4.202	4.189
LiCl	4.972	4.967	5.157	5.082	5.074	5.099	5.097	5.069	5.094	5.093	5.095	4.996	5.070
LiF	3.926	3.913	4.080	4.010	3.998	4.011	4.011	3.989	4.013	4.010	4.007	3.978	3.972
Al	3.987	3.983	4.044	4.042	4.037	4.053	4.051	4.041	4.048	4.050	4.051	4.050	4.018
Na	4.054	4.056	4.197	4.205	4.182	4.229	4.225	4.221	4.233	4.232	4.257	4.232	4.214
Cu	3.530	3.523	3.643	3.622	3.597	3.612	3.616	3.622	3.625	3.625	3.626	3.625	3.595
Pd	3.839	3.830	3.941	3.914	3.896	3.919	3.918	3.916	3.920	3.920	3.918	3.920	3.876
% M.A.E.	1.2	1.3	1.3	0.6	0.5	0.7	0.7	0.5	0.7	0.7	0.7	0.6	...
	LDA	LDA ^a	PBE	RPA	RPA ^a	rALDA	rALDAc	CDOP	CDOPs	CP	CPd	JGMs	Expt.
C	465	465	432	435	441	439	440	443	439	439	448	455	443
Si	95	97	88	95	99	95	95	96	95	95	99	98	99
SiC	228	229	211	220	223	220	221	223	221	221	224	231	225
MgO	172	172	151	163	168	161	161	164	161	162	163	174	165
LiCl	41	41	31	36	37	35	35	38	36	36	35	40	35
LiF	86	87	67	71	76	71	71	77	72	72	72	72	70
Al	83	84	77	78	77	76	76	78	76	76	75	76	79
Na	9	9	8	8	8	8	8	8	8	8	7	8	8
Cu	184	186	136	156	153	156	156	155	151	151	152	151	142
Pd	226	226	169	199	181	195	196	196	194	194	192	194	195
% M.A.E.	12	12	7	3	3	3	3	4	3	3	3	4	...

^aReference 46.

From this convergence behavior, we conclude that the short-range description of correlation obtained from an XC-kernel like the rALDA is easier to describe in a plane-wave basis than the erroneous short-range behavior of the RPA. This result might have been anticipated from the HEG, where the coupling-constant averaged pair-distribution function calculated for the rALDA is softer than for the RPA (Fig. 2).

4. CP and CDOPs

The CP and CDOPs kernels yield lattice constants and bulk moduli which are also very similar to each other across the full range of systems. This behavior can be explained by considering Fig. 1(a), where it can be seen that f_{xc}^{CDOPs} lies more negative than f_{xc}^{CP} for k less than $\sim 2k_F$, and more positive otherwise. The kernel averaging procedure smears out these differences. In particular, there is a negligible effect from modifying the large- k behavior from $-4\pi B/k^2$ (CDOPs) to $-4\pi/k^2$ (CP).

f_{xc}^{CDOPs} and f_{xc}^{CP} closely follow the rALDA kernels (and the RPA) for non-metallic systems. For metallic systems, differences of order 0.3% can be observed. The most likely reason for this difference is the long-range behavior of the rALDA kernels, which display decaying oscillations, compared to the CDOPs and CP kernels which go to zero more smoothly. The small positive hump displayed by the CDOPs kernel in real

space [Fig. 1(b)] appears to have little effect on the correlation energy.

5. CDOP

The CDOP kernel (Eq. (17)) differs from f_{xc}^{CDOPs} by having a local term. This local term has a noticeable effect on the calculated structural properties, with the CDOP kernel predicting slightly smaller and larger lattice constants and bulk moduli, respectively. Indeed, the CDOP kernel displays the closest agreement with experimental lattice constants, but performs less well on bulk moduli.

In Sec. II C 4, it was pointed out that the local term in the CDOP kernel leads to a divergent pair-distribution function. The local term may also be expected to introduce convergence problems, as demonstrated for the (entirely local) ALDA kernel.^{27,30} In the current work, we have not found any significant difference in the convergence behavior of the CDOP and CDOPs kernels when calculating lattice constants and bulk moduli for $E_{cut} \leq 400$ eV. Only in cases where the RPA correlation energy converges relatively quickly (e.g., Al), we can observe a slowly converging positive contribution to the CDOP correlation energy which is reminiscent of that found for the ALDA, cf. Fig. 3 of Ref. 30. However, unlike for the ALDA, the magnitude of this contribution is very small compared to the RPA-like convergence (e.g., Fig. 3).

6. CPd

The dynamical CPd kernel displays slight differences to its $\omega = 0$ limit, f_{xc}^{CP} . Compared to the static kernels where the range of f_{xc} is fixed by the density, for the CPd kernel, the frequency appearing in the denominator of χ_{KS} also affects the range. Interestingly, the CPd bulk moduli of insulators are slightly closer to experiment. In other cases, we find that the CP and CPd kernels predict similar results except for Na, where the CPd kernel finds a larger lattice constant and smaller bulk modulus, and C, where the CPd lattice constant lies on top of the experimental value.

The CPd results show that even a simple dynamical kernel can predict different structural properties. This result is not obvious from studies on the HEG, where tests on the more complicated frequency-dependent kernel of Ref. 18 found dynamical effects to be less important than nonlocality when calculating correlation energies.¹⁵ Although we do not observe systematic improvement with the CPd kernel, it would be interesting to investigate its performance for systems with a greater degree of inhomogeneity, e.g., molecules and surfaces.

7. JGMs

The lattice constants calculated with the JGMs kernel for insulating systems display the closest agreement with experiment out of all of the considered kernels, except for the notable example of LiCl, where the JGMs lattice constant is underestimated by 1.4%. However the agreement with experimental bulk moduli is poorer, in some cases (SiC, MgO) worse than the LDA. For metallic systems, the JGMs and CP kernels coincide.

It is important to establish the importance of the value of E_g . In the current work, we have used the experimental, direct gap (Table II), but we equally could have chosen the indirect gap or even defined a more general \mathbf{r} -dependent gap function.⁹⁸ An alternative option is to make the link to the description of excitons^{38,70} and consider the head ($\mathbf{G} = \mathbf{G}' = 0$) of f_{xc}^{JGMs} in the $q \rightarrow 0$ limit, which can be written as $-\langle\alpha\rangle/q^2$, where

$$\langle\alpha\rangle = \frac{4\pi}{\Omega} \int_{\Omega} d\mathbf{r} \left[1 - e^{-E_g^2/[4\pi n(\mathbf{r})]} \right]. \quad (40)$$

The values of $\langle\alpha\rangle$ computed from Eq. (40) for the experimental gaps are given in Table II. These values can be compared

TABLE II. Parameters relating to the JGMs kernel. The values of $\langle\alpha\rangle$ were obtained by inserting the experimental band gaps E_g into Eq. (40), while inserting the “effective gaps” E_g^{eff} yields the α_{LRC} values reported in Ref. 70 (these calculations were performed at the experimental lattice constant). The α_{LRC} values for LiCl and LiF were obtained from Eq. (4) of Ref. 70 using the dielectric constants tabulated in Ref. 91. The experimental (direct) band gaps were obtained from Refs. 92–97.

	C	Si	SiC	MgO	LiCl	LiF
E_g (eV)	7.3	3.4	6.0	7.8	9.4	14.2
$\langle\alpha\rangle$	0.58	0.89	1.30	2.32	5.60	7.03
E_g^{eff} (eV)	7.43	1.57	3.62	6.74	3.98	6.07
α_{LRC}	0.6	0.2	0.5	1.8	1.5	2.2

to Ref. 70, where a long-range (LRC) attractive kernel was introduced as $f_{xc}(R) = -\alpha_{\text{LRC}}/(4\pi R)$. We note that the head of this matrix in reciprocal space in the $q \rightarrow 0$ limit coincides with the JGMs kernel with $\alpha_{\text{LRC}} \rightarrow \langle\alpha\rangle$, and also that this single matrix element is considered the most important for the calculation of excitonic effects.⁷⁰

From Table II, it is clear that the values of $\langle\alpha\rangle$ calculated with the experimental gaps and PAW densities are somewhat larger than the values of α_{LRC} reported in Ref. 70, which were found to give a good description of excitonic effects in absorption spectra of semiconductors and MgO. To explore this point, further, we adopted an inverse approach and considered an effective gap E_g^{eff} , which when inserted into Eq. (40) yields α_{LRC} . These LRC “gaps” are smaller than experimental values, especially for the ionic compounds. Indeed, the empirical α_{LRC} values of LiCl and LiF are significantly smaller than those expected both from the JGM or bootstrap kernels,^{38,71} which have been shown to accurately capture the exciton in LiF.

We repeated the JGMs kernel calculations using the LRC gaps E_g^{eff} and show the obtained lattice constants in Fig. 6. The LRC results lie between the lattice constants calculated with the RPA and with the JGMs kernel/experimental gaps, and thus improve the LiCl result. Comparison of LiCl and LiF demonstrates the nonlinear relation between E_g^{eff} and the lattice constant. In both cases, the effective gap is reduced by more than 50% from its experimental value, but the effect on the LiCl lattice constant is an order of magnitude larger than for LiF.

The improved agreement of lattice constants with experiment compared to the RPA shows that XC-kernels with long-range components represent an interesting avenue to study. A key question is whether the tendency for the JGMs kernel to favor smaller lattice constants than the RPA is directly related to the fundamental long-range character of the former, or whether it is in fact a consequence of the precise form of the kernel. The strength of the long-range part of the JGMs

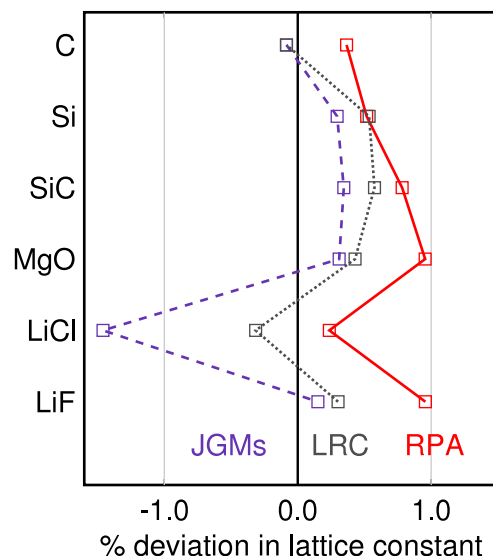


FIG. 6. Percentage deviations of lattice constants compared to experiment,⁴⁶ calculated with the RPA, and the JGMs kernel using the experimental direct band gaps or effective LRC gaps (see Table II).

Hartree-XC kernel is determined by $\exp(-E_g^2/4\pi n)$ (Eq. (23)), which becomes RPA-like in the high density limit and vanishes in the low density limit. The RPA correlation energy is generally negative, while a zero f_{Hxc} implies a zero correlation energy. Interpolating these two limits implies that a more negative (i.e., stable) JGMs correlation energy will correspond to a higher density, thus favoring a lower lattice constant. This observation also provides an explanation for the varying behavior of the bulk modulus and also the strong nonlinearity in the variation of the lattice constant with band gap, since the energy-volume relation is expected to be sensitive to the relative magnitude of E_g and n .

We note that the bootstrap approach⁷¹ is an alternative method of constructing a long-range kernel. Since the bootstrap kernel is constructed from χ_{KS} , using it would avoid both the input of E_g and the averaging procedures discussed in Sec. II G. However, it would be necessary to ensure that the bootstrap kernel displayed reasonable behavior in the large k -limit.

B. Absolute correlation energies

In Fig. 7, we show the absolute correlation energy per electron calculated using each of the different kernels for the materials in the test set. Absolute correlation energies are generally considered less robust than properties constructed from energy differences, being more difficult to converge and sensitive to details of the PAW potentials. However, one can still perform a comparison between kernels and look for similarities with the trends observed for the HEG [Fig. 1(d)].

The most obvious feature of Fig. 7 is the reduction of absolute correlation energy on moving from the RPA to a nonzero f_{xc} , ranging from 0.1 eV for Na to 0.5 eV for Si. This change is the same order of magnitude as observed for the HEG. The ordering of the HEG correlation energy calculated with different kernels is also largely preserved, with the CP and CDOPs kernels predicting larger magnitudes than CDOP and the rALDA kernels.

The difference between the rALDA and rALDAc kernels is small, with the rALDA correlation energy being more negative by order 1% or 0.01 eV per electron. The difference between the static and dynamical forms of the CP kernel is an order of magnitude larger, with the static correlation energy being more negative. Meanwhile, the removal of the local term in the CDOP kernel increases the magnitude of the correlation

energy, with the CDOPs having a more negative correlation energy than CDOP by 5% or 0.05 eV per electron.

As in Ref. 29, we can tentatively compare our calculated correlation energy for Si with the diffusion Monte Carlo (DMC) calculations of Ref. 99. Reassuringly the DMC correlation energy lies among the values calculated with the model exchange kernels (Fig. 7), in fact displaying closest agreement with CPd, rALDA, and CDOP kernels. We also note that our calculated CDOP correlation energy for Si (−1.02 eV per electron) lies on top of the value recently reported in Ref. 29 using a pseudopotential approximation and a different averaging scheme (Eq. (37)). With highly accurate calculations of correlation energies in extended systems now becoming a reality,¹⁰⁰ comparisons of this sort should become a useful test for new kernels.

C. Kernel averaging scheme

It is interesting to compare the structural properties and correlation energies calculated using the symmetrized-wavevector averaging scheme (Eq. (38)) to the two-point symmetrized density (Eq. (34)). The latter has previously been implemented for the rALDA,³¹ so here we restrict the comparison to this kernel.

Considering the lattice constants first, we typically find a difference of 0.2% between the two methods, with the symmetrized-density values larger than those calculated with the symmetrized-wavevector in most cases. Interestingly, the agreement is worse for the bulk moduli, with an average deviation of 6%. The absolute correlation energies also show a larger (4%) deviation, where using the two-point symmetrized density scheme consistently yields more negative rALDA correlation energies than the symmetrized-wavevector scheme, by an average of 0.04 eV per electron.

To understand the origin of these differences, it is necessary to consider the practical implementation of the two-point density average (Eq. (34)). As mentioned in Sec. II G, constructing the kernel in this way involves sampling the $1/R$ Coulomb interaction in real space. The divergence at $R = 0$ is replaced with a spherical average of $1/R$ taken over the volume per point in the real-space grid used to evaluate the integral.³¹ The absolute correlation energy is therefore rather sensitive to this grid spacing, and its dependence on volume (i.e., the bulk modulus) will also be difficult to converge.

The symmetrized-wavevector approach only samples the density on the real space grid, and therefore shows a much

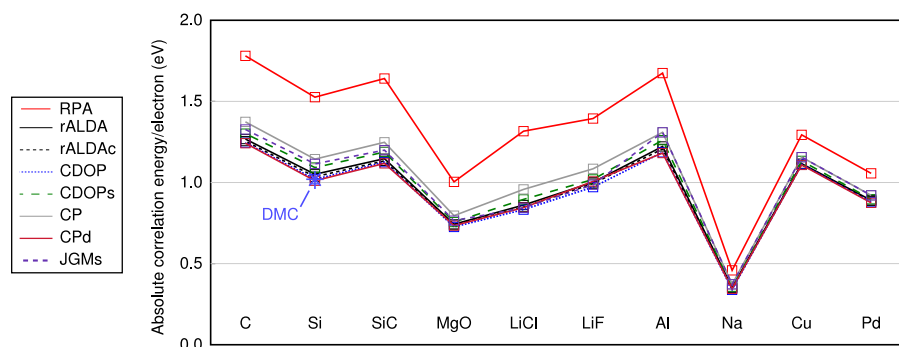


FIG. 7. Absolute correlation energies E_c (Eq. (1)) calculated per (valence) electron for different kernels. The correlation energy obtained for Si from the DMC calculations of Ref. 99 is also shown. The core/valence partitioning of the PAW potentials is given in Ref. 85. The calculations were performed at the experimental lattice constant.

weaker dependence on the spacing between the grid points. We verified this behavior for diamond C, where the symmetrized-wavevector correlation energy changes by less than 10^{-5} eV/electron on reducing the grid spacing from 0.17 to 0.11 Å. This is several orders of magnitude faster than the symmetrized-density approach,³¹ illustrating a computational advantage of Eq. (38).

D. Spin and atomization energies: The H₂ molecule

Throughout this study, we have not considered any spin-dependence of the XC-kernels. However, the calculation of atomization or cohesive energies usually requires the description of spin-polarized atoms or molecules. In this section, we provide a demonstration of the importance of spin by calculating the atomization energy of the H₂ molecule with the rALDA kernel.

First, we note that the symmetrized-wavevector averaging procedure (Eq. (38)) can be equally applied to extended and finite systems. In fact, for the rALDA kernel, one can exploit the fact that the Hartree-XC kernel strictly vanishes at any points in space where the density is less than $(|\mathbf{G} + \mathbf{q}||\mathbf{G}' + \mathbf{q}|)^{3/2}/(24\pi^2)$. Therefore, the Fourier transform can be performed in a small box which excludes the vacuum region generally required to model isolated systems with periodic boundary conditions. Since the H₂ molecule is spin-unpolarized, we can calculate its correlation energy without any further consideration and obtain a value of -1.04 eV with the rALDA kernel. This value is within 0.1 eV of the value obtained from coupled-cluster calculations¹⁰¹ and a significant improvement (>1 eV) over the RPA. We find a similar level of agreement for the He atom (Table III).

For the spin-polarized H atom, following the analysis of Ref. 31, we replace the integral equation (Eq. (3)) with its the spin-polarized version, valid for systems where only one spin channel is occupied,

$$\chi^{\uparrow\uparrow}(\mathbf{q}, \omega) = \chi_{\text{KS}}^{\uparrow}(\mathbf{q}, \omega) + \chi_{\text{KS}}^{\uparrow}(\mathbf{q}, \omega) f_{Hxc}^{\uparrow\uparrow}(\mathbf{q}, \omega) \chi^{\uparrow\uparrow}(\mathbf{q}, \omega). \quad (41)$$

The above quantities are related to Eq. (1) through the simple substitutions $\chi \rightarrow \chi^{\uparrow\uparrow}$ and $\chi_{\text{KS}} \rightarrow \chi_{\text{KS}}^{\uparrow}$.

Proceeding further requires the spin-polarized form of the Hartree-XC kernel $f_{Hxc}^{\uparrow\uparrow}(\mathbf{q}, \omega)$. To our knowledge, of the XC-kernels studied in this work, $f_{Hxc}^{\uparrow\uparrow}$ has been derived only for

the rALDA, given as³¹

$$f_{Hxc}^{\uparrow\uparrow}(k) = \frac{4\pi}{k^2} - \left[2 \times \theta(k_c - k) \frac{4\pi}{k_c^2} + \theta(k - k_c) \frac{4\pi}{k^2} \right]. \quad (42)$$

Equation (42) differs from the spin-unpolarized rALDA expression (Eq. (14)) by a factor of two in front of the part of the kernel corresponding to the ALDA, reflecting the fact that the exchange interaction acts only between electrons with the same spin. Using Eqs. (41) and (42) to calculate the correlation energy of the H atom yields a value of 0.06 eV, compared to the exact value of zero and an RPA value of -0.57 eV.

Taking the H and H₂ calculations together yields an rALDA atomization energy of 4.82 eV, which is within 0.1 eV of the experimental value of 4.75 eV.¹⁰² We note that the RPA benefits from substantial error cancellation and yields an atomization energy very close to experiment (4.74 eV, Table III). However, the H₂ molecule is a rather special case, and the RPA usually demonstrates percentage errors of order 10% in atomization energies.³² The rALDA kernel corrects the correlation energies of the individual H₂ and H systems and maintains close agreement with the experimental atomization energy.

In Table III, we also present the rALDA correlation energies using the two-point density average, Eq. (34). As found in bulk systems, the correlation energies calculated with the two-point density average are more negative (~ 0.06 eV/electron) than those calculated with the symmetrized wavevector. However, the agreement in atomization energies is better than 0.03 eV. We find it encouraging that the symmetrized-wavevector approach gives such similar results to the more intuitive two-point density average when calculating the atomization energy.

We note that if we do not use the spin-polarized form of the kernel (Eq. (42)), we find a correlation energy of -0.17 eV for the H atom and an atomization energy of 4.37 eV. This value is in significantly worse agreement with experiment than the RPA or even the LDA (4.89 eV), emphasizing the importance of a rigorous treatment of spin. An important direction for further study is the introduction of spin-dependence into kernels derived from the spin-unpolarized HEG.

IV. CONCLUSIONS

We have calculated the correlation energy of a test set of 10 materials within the ACFD-DFT. We used a hierarchy of approximations for the XC kernel f_{xc} , including the random phase approximation ($f_{xc} = 0$), the recently introduced renormalized kernels (rALDA),³¹ a kernel which satisfies the exact static limits of the electron gas (CDOP),¹⁷ a model dynamical kernel (CPd),¹⁶ and a kernel which diverges $\propto 1/k^2$ in the small- k limit (JGMs).³⁸ In order to apply homogeneous kernels to inhomogeneous systems, we applied a reciprocal space averaging scheme employing wavevector symmetrization.³⁸ For each kernel and material pair, we calculated the lattice constant and bulk modulus and compared our results to previous calculations and experiment.⁴⁶

For all materials, including a nonzero f_{xc} reduces the magnitude of the correlation energy compared to the RPA by

TABLE III. Correlation energies of H, H₂, and He and the atomization energy of the H₂ molecule [$E_{\text{at}}(\text{H}_2)$] calculated at different levels of theory. The CCSD values are taken from Ref. 101 and the experimental atomization energy from Ref. 102. The rALDA results were calculated including spin-polarization, with the kernels constructed either from Eq. (38) or Eq. (34). All values are given in eV.

	RPA	rALDA ^a	rALDA ^b	CCSD	Expt.
H	-0.57	0.06	-0.02	0.00	...
H ₂	-2.22	-1.04	-1.22	-1.11	...
He	-1.82	-1.00	-1.08	-1.14	...
$E_{\text{at}}(\text{H}_2)$	4.74	4.82	4.85	4.75	4.75

^aSymmetrized wavevector, Eq. (38).

^bSymmetrized density, Eq. (34).

0.1–0.5 eV per electron. This result mirrors the HEG, where the RPA correlation energy is too negative by at least 0.3 eV over a wide range of densities.¹⁵ However, the variation in correlation energy between each f_{xc} is much smaller, on the scale of 0.01–0.1 eV per electron. Encouragingly, the correlation energies calculated with XC-kernels are found to lie very close to diffusion Monte Carlo data available for Si.⁹⁹ Furthermore, calculations with XC-kernels display faster basis-set convergence than the RPA due to the suppression of high energy plane-wave components of the Coulomb potential.

Considering lattice constants and bulk moduli, we found only small variations between the RPA and different XC-kernels. In particular, static XC-kernels that only satisfy the $k \rightarrow 0$, $\omega = 0$ limit of the HEG (rALDA, CP, CDOPs) produce very similar results. The structural properties calculated with the dynamical CPd kernel are in better agreement with experiment in some cases (e.g., the bulk moduli of non-metallic systems), but the improvement is not systematic (e.g., Na). Satisfying the $k \rightarrow \infty$, $\omega = 0$ limit of the HEG (which adds a local term to f_{xc} , e.g., the CDOP kernel) also yields good agreement with experimental lattice constants, despite the kernel having a diverging pair-distribution function.²⁹ Finally, the JGMs kernel predicts a reduction in lattice constants and an increase in bulk moduli for non-metallic systems, bringing the former into closer agreement with experiment. The current study however cannot distinguish whether this behavior is due to the general long-range $-\alpha/(4\pi R)$ character of the kernel,⁷⁰ or to the density-dependence of α specific to the JGMs model.³⁸

The ACFD-DFT scheme described here clearly involves a number of choices, including (a) the approximation used to generate the noninteracting response function χ_{KS} , (b) the form of f_{xc} (including spin-dependence), and (c) the averaging scheme used to generalize a HEG XC-kernel to an inhomogeneous system. Fixing all factors except (b), as we have done here, points us towards the essential properties of a model f_{xc} . Based on the similar performance of the different XC-kernels, the current work supports the idea that f_{xc} should be kept as simple as possible, i.e., be static, tend to a density-dependent constant at small k , and decay $\propto 1/k^2$ at large k . In this respect, the exchange-only rALDA kernel is attractive, since it scales simply with the coupling constant λ and has good convergence properties. The introduction of additional computational expense and uncertainty associated with a dynamical kernel, a divergence $\propto 1/k^2$ at $k = 0$ or even a local term in f_{xc} , is difficult to justify based on the performance of the CPd, JGMs, and CDOP kernels for lattice constants and bulk moduli, although each kernel was found to offer improved agreement with experiment in certain cases.

On the other hand, by focusing on the structural properties of bulk solids, we have chosen systems where the RPA already performs very well. It is encouraging that the model XC-kernels can maintain this good performance whilst correcting the magnitude of the correlation energy by several eV per atom, but arguably their real test lies in cases where the RPA is less successful. Already, the rALDA kernel has been found to improve the description of atomization and cohesive energies^{31,32} but a number of challenges remain, particularly in the description of molecular dissociation.^{46,75,103,104} The framework described in the current study provides the base

for the application of a full range of kernels to these more challenging systems.

ACKNOWLEDGMENTS

We thank T. Olsen and J. J. Mortensen for useful advice and discussions, and D. Lu for helpful correspondence. The authors acknowledge support from the Danish Council for Independent Research's Sapere Aude Program, Grant No. 11-1051390.

- ¹P. Hohenberg and W. Kohn, *Phys. Rev.* **136**, B864 (1964).
- ²W. Kohn and L. J. Sham, *Phys. Rev.* **140**, A1133 (1965).
- ³A. D. Becke, *J. Chem. Phys.* **140**, 18A301 (2014).
- ⁴D. C. Langreth and J. P. Perdew, *Phys. Rev. B* **15**, 2884 (1977).
- ⁵O. Gunnarsson and B. I. Lundqvist, *Phys. Rev. B* **13**, 4274 (1976).
- ⁶X. Ren, P. Rinke, C. Joas, and M. Scheffler, *J. Mater. Sci.* **47**, 7447 (2012).
- ⁷A. Marini, P. García-González, and A. Rubio, *Phys. Rev. Lett.* **96**, 136404 (2006).
- ⁸A. Ruzsinszky, J. P. Perdew, and G. I. Csonka, *J. Chem. Phys.* **134**, 114110 (2011).
- ⁹A. Heßelmann and A. Görling, *Phys. Rev. Lett.* **106**, 093001 (2011).
- ¹⁰D. L. Freeman, *Phys. Rev. B* **15**, 5512 (1977).
- ¹¹J. Paier, B. G. Janesko, T. M. Henderson, G. E. Scuseria, A. Grneis, and G. Kresse, *J. Chem. Phys.* **132**, 094103 (2010).
- ¹²Y. Niquet, M. Fuchs, and X. Gonze, *Phys. Rev. A* **68**, 032507 (2003).
- ¹³E. Runge and E. K. U. Gross, *Phys. Rev. Lett.* **52**, 997 (1984).
- ¹⁴M. Petersilka, U. J. Gossmann, and E. K. U. Gross, *Phys. Rev. Lett.* **76**, 1212 (1996).
- ¹⁵M. Lein, E. K. U. Gross, and J. P. Perdew, *Phys. Rev. B* **61**, 13431 (2000).
- ¹⁶L. A. Constantin and J. M. Pitarke, *Phys. Rev. B* **75**, 245127 (2007).
- ¹⁷M. Corradini, R. Del Sole, G. Onida, and M. Palumbo, *Phys. Rev. B* **57**, 14569 (1998).
- ¹⁸C. F. Richardson and N. W. Ashcroft, *Phys. Rev. B* **50**, 8170 (1994).
- ¹⁹J. Pitarke and A. Eguiluz, *Phys. Rev. B* **63**, 045116 (2001).
- ²⁰J. Pitarke and J. Perdew, *Phys. Rev. B* **67**, 045101 (2003).
- ²¹J. F. Dobson and J. Wang, *Phys. Rev. B* **62**, 10038 (2000).
- ²²J. Jung, P. García-González, J. F. Dobson, and R. W. Godby, *Phys. Rev. B* **70**, 205107 (2004).
- ²³L. Constantin and J. Pitarke, *Phys. Rev. B* **83**, 075116 (2011).
- ²⁴L. Constantin, L. Chiodo, E. Fabiano, I. Bodrenko, and F. Della Sala, *Phys. Rev. B* **84**, 045126 (2011).
- ²⁵J. Pitarke, L. Constantin, and J. Perdew, *Phys. Rev. B* **74**, 045121 (2006).
- ²⁶M. Hellgren and U. von Barth, *Phys. Rev. B* **78**, 115107 (2008).
- ²⁷F. Furche and T. Van Voorhis, *J. Chem. Phys.* **122**, 164106 (2005).
- ²⁸T. Gould and J. Dobson, *Phys. Rev. A* **85**, 062504 (2012).
- ²⁹D. Lu, *J. Chem. Phys.* **140**, 18A520 (2014).
- ³⁰T. Olsen and K. S. Thygesen, *Phys. Rev. B* **86**, 081103(R) (2012).
- ³¹T. Olsen and K. S. Thygesen, *Phys. Rev. B* **88**, 115131 (2013).
- ³²T. Olsen and K. S. Thygesen, *Phys. Rev. Lett.* **112**, 203001 (2014).
- ³³S. Ichimaru, *Rev. Mod. Phys.* **54**, 1017 (1982).
- ³⁴A. Holas, in *Strongly Coupled Plasma Physics*, edited by F. J. Rogers and H. E. Dewitt (Plenum Press, New York, 1987), pp. 463–482.
- ³⁵E. K. U. Gross and W. Kohn, *Phys. Rev. Lett.* **55**, 2850 (1985).
- ³⁶W. G. Aulbur, L. Jönsson, and J. W. Wilkins, *Phys. Rev. B* **54**, 8540 (1996).
- ³⁷P. Ghosez, X. Gonze, and R. W. Godby, *Phys. Rev. B* **56**, 12811 (1997).
- ³⁸P. E. Trevisanuto, A. Terentjev, L. A. Constantin, V. Olevario, and F. Della Sala, *Phys. Rev. B* **87**, 205143 (2013).
- ³⁹M. Lein and E. Gross, in *Time-Dependent Density Functional Theory*, Lecture Notes in Physics Vol. 706, edited by M. A. L. Marques, C. A. Ullrich, F. Nogueira, A. Rubio, K. Burke, and E. K. U. Gross (Springer, Berlin, Heidelberg, 2006), pp. 423–434.
- ⁴⁰D. Pines and P. Nozières, *The Theory of Quantum Liquids* (W. A. Benjamin, Inc., New York, 1966).
- ⁴¹J. Yan, J. J. Mortensen, K. W. Jacobsen, and K. S. Thygesen, *Phys. Rev. B* **83**, 245122 (2011).
- ⁴²F. Furche, *Phys. Rev. B* **64**, 195120 (2001).
- ⁴³M. Fuchs and X. Gonze, *Phys. Rev. B* **65**, 235109 (2002).
- ⁴⁴D. Lu, Y. Li, D. Rocca, and G. Galli, *Phys. Rev. Lett.* **102**, 206411 (2009).
- ⁴⁵H.-V. Nguyen and S. de Gironcoli, *Phys. Rev. B* **79**, 205114 (2009).
- ⁴⁶J. Harl, L. Schimka, and G. Kresse, *Phys. Rev. B* **81**, 115126 (2010).

- ⁴⁷L. Schimka, J. Harl, A. Stroppa, A. Grüneis, M. Marsman, F. Mittendorfer, and G. Kresse, *Nat. Mater.* **9**, 741 (2010).
- ⁴⁸T. Olsen, J. Yan, J. J. Mortensen, and K. S. Thygesen, *Phys. Rev. Lett.* **107**, 156401 (2011).
- ⁴⁹T. Olsen and K. S. Thygesen, *Phys. Rev. B* **87**, 075111 (2013).
- ⁵⁰L. Hedin and S. Lundqvist, in *Solid State Physics*, edited by F. Seitz, D. Turnbull, and H. Ehrenreich (Academic Press, 1970), Vol. 23, pp. 1–181.
- ⁵¹M. S. Hybertsen and S. G. Louie, *Phys. Rev. B* **34**, 5390 (1986).
- ⁵²R. W. Godby, M. Schlüter, and L. J. Sham, *Phys. Rev. B* **37**, 10159 (1988).
- ⁵³T. Kotani, *J. Phys.: Condens. Matter* **10**, 9241 (1998).
- ⁵⁴N. L. Nguyen, N. Colonna, and S. de Gironcoli, *Phys. Rev. B* **90**, 045138 (2014).
- ⁵⁵J. Klimeš and G. Kresse, *J. Chem. Phys.* **140**, 054516 (2014).
- ⁵⁶Reference 27 notes that a lack of consistency between v_{xc} and the f_{xc} used in Eq. (3) may yield pathological results for spin-polarized molecules, but this effect is not expected to occur for the systems considered here.
- ⁵⁷J. C. Inkson, *Many-Body Theory of Solids* (Plenum Press, New York, 1984).
- ⁵⁸B. Farid, V. Heine, G. E. Engel, and I. J. Robertson, *Phys. Rev. B* **48**, 11602 (1993).
- ⁵⁹G. Niklasson, *Phys. Rev. B* **10**, 3052 (1974).
- ⁶⁰G. Vignale, *Phys. Rev. B* **38**, 6445 (1988).
- ⁶¹J. Toulouse, *Phys. Rev. B* **72**, 035117 (2005).
- ⁶²G. Ortiz and P. Ballone, *Phys. Rev. B* **50**, 1391 (1994).
- ⁶³J. P. Perdew and Y. Wang, *Phys. Rev. B* **45**, 13244 (1992).
- ⁶⁴S. Moroni, D. M. Ceperley, and G. Senatore, *Phys. Rev. Lett.* **75**, 689 (1995).
- ⁶⁵J. C. Kimball, *Phys. Rev. A* **7**, 1648 (1973).
- ⁶⁶K. S. Singwi, A. Sjölander, M. P. Tosi, and R. H. Land, *Phys. Rev. B* **1**, 1044 (1970).
- ⁶⁷J. P. Perdew and Y. Wang, *Phys. Rev. B* **46**, 12947 (1992).
- ⁶⁸J. P. Perdew and Y. Wang, *Phys. Rev. B* **56**, 7018 (1997).
- ⁶⁹D. M. Ceperley and B. J. Alder, *Phys. Rev. Lett.* **45**, 566 (1980).
- ⁷⁰S. Botti, F. Sottile, N. Vast, V. Olevano, L. Reining, H.-C. Weissker, A. Rubio, G. Onida, R. Del Sole, and R. W. Godby, *Phys. Rev. B* **69**, 155112 (2004).
- ⁷¹S. Sharma, J. K. Dewhurst, A. Sanna, and E. K. U. Gross, *Phys. Rev. Lett.* **107**, 186401 (2011).
- ⁷²F. Sottile, K. Karlsson, L. Reining, and F. Aryasetiawan, *Phys. Rev. B* **68**, 205112 (2003).
- ⁷³Z. H. Levine and S. G. Louie, *Phys. Rev. B* **25**, 6310 (1982).
- ⁷⁴D. R. Penn, *Phys. Rev.* **128**, 2093 (1962).
- ⁷⁵J. Toulouse, I. C. Gerber, G. Jansen, A. Savin, and J. G. Ángyán, *Phys. Rev. Lett.* **102**, 096404 (2009).
- ⁷⁶B. G. Janesko, T. M. Henderson, and G. E. Scuseria, *J. Chem. Phys.* **130**, 081105 (2009).
- ⁷⁷F. Bruneval, *Phys. Rev. Lett.* **108**, 256403 (2012).
- ⁷⁸J. Klimeš, M. Kaltak, and G. Kresse, *Phys. Rev. B* **90**, 075125 (2014).
- ⁷⁹K. Burke, in *Time-Dependent Density Functional Theory*, Lecture Notes in Physics Vol. 706, edited by M. A. L. Marques, C. A. Ullrich, F. Nogueira, A. Rubio, K. Burke, and E. K. U. Gross (Springer, Berlin, Heidelberg, 2006), pp. 181–194.
- ⁸⁰P. García-González, J. E. Alvarellos, and E. Chacón, *Phys. Rev. A* **54**, 1897 (1996).
- ⁸¹R. Cuevas-Saavedra, D. Chakraborty, S. Rabi, C. Cárdenas, and P. W. Ayers, *J. Chem. Theory Comput.* **8**, 4081 (2012).
- ⁸²J. Enkovaara *et al.*, *J. Phys.: Condens. Matter* **22**, 253202 (2010).
- ⁸³P. E. Blöchl, *Phys. Rev. B* **50**, 17953 (1994).
- ⁸⁴H. J. Monkhorst and J. D. Pack, *Phys. Rev. B* **13**, 5188 (1976).
- ⁸⁵Our PAW potentials had the following numbers of valence electrons: H, 1; He, 2; Li, 3; Na, 7; Mg, 10; Al, 3; Cu, 11; Pd, 16; C, 4; Si, 4; O, 6; F, 7; Cl, 7.
- ⁸⁶G. Román-Pérez and J. M. Soler, *Phys. Rev. Lett.* **103**, 096102 (2009).
- ⁸⁷F. Birch, *Phys. Rev.* **71**, 809 (1947).
- ⁸⁸R. Sundararaman and T. A. Arias, *Phys. Rev. B* **87**, 165122 (2013).
- ⁸⁹F. Labat, E. Brémond, P. Cortona, and C. Adamo, *J. Mol. Model.* **19**, 2791 (2013).
- ⁹⁰J. P. Perdew, K. Burke, and M. Ernzerhof, *Phys. Rev. Lett.* **77**, 3865 (1996).
- ⁹¹N. W. Ashcroft and N. D. Mermin, *Solid State Physics* (Saunders, Philadelphia, 1976).
- ⁹²R. A. Roberts and W. C. Walker, *Phys. Rev.* **161**, 730 (1967).
- ⁹³R. R. L. Zucca and Y. R. Shen, *Phys. Rev. B* **1**, 2668 (1970).
- ⁹⁴W. J. Choyke and L. Patrick, *Phys. Rev.* **187**, 1041 (1969).
- ⁹⁵R. Whited, C. J. Flaten, and W. Walker, *Solid State Commun.* **13**, 1903 (1973).
- ⁹⁶F. C. Brown, C. Gähwiller, H. Fujita, A. B. Kunz, W. Scheifley, and N. Carrera, *Phys. Rev. B* **2**, 2126 (1970).
- ⁹⁷M. Piacentini, D. W. Lynch, and C. G. Olson, *Phys. Rev. B* **13**, 5530 (1976).
- ⁹⁸E. Fabiano, P. E. Trevisanutto, A. Terentjev, and L. A. Constantin, *J. Chem. Theory Comput.* **10**, 2016 (2014).
- ⁹⁹R. Q. Hood, M. Y. Chou, A. J. Williamson, G. Rajagopal, and R. J. Needs, *Phys. Rev. B* **57**, 8972 (1998).
- ¹⁰⁰G. H. Booth, A. Grüneis, G. Kresse, and A. Alavi, *Nature* **493**, 365 (2013).
- ¹⁰¹J. S. Lee and S. Y. Park, *J. Chem. Phys.* **112**, 10746 (2000).
- ¹⁰²A. Karton, E. Rabinovich, J. M. L. Martin, and B. Ruscic, *J. Chem. Phys.* **125**, 144108 (2006).
- ¹⁰³P. Mori-Sánchez, A. J. Cohen, and W. Yang, *Phys. Rev. A* **85**, 042507 (2012).
- ¹⁰⁴T. M. Henderson and G. E. Scuseria, *Mol. Phys.* **108**, 2511 (2010).